Dark Energy Survey Year 3 Results: Constraints on cosmological parameters and galaxy bias models from galaxy clustering and galaxy-galaxy lensing using the `redMaGiC` sample

S. Pandey,[1, *] E. Krause,[2] J. DeRose,[3] N. MacCrann,[4] B. Jain,[1] M. Crocce,[5, 6] J. Blazek,[7, 8] A. Choi,[9] H. Huang,[10] C. To,[11, 12, 13]
X. Fang,[2] J. Elvin-Poole,[9, 14] J. Prat,[15, 16] A. Porredon,[9, 14] L. F. Secco,[1, 16] M. Rodriguez-Monroy,[17] N. Weaverdyck,[18] Y. Park,[19]
M. Raveri,[1] E. Rozo,[10] E. S. Rykoff,[12, 13] G. M. Bernstein,[1] C. Sánchez,[1] M. Jarvis,[1] M. A. Troxel,[20] G. Zacharegkas,[16]
C. Chang,[15, 16] A. Alarcon,[21] O. Alves,[18, 22, 23] A. Amon,[12] F. Andrade-Oliveira,[22, 23] E. Baxter,[24] K. Bechtol,[25] M. R. Becker,[21]
H. Camacho,[22, 23] A. Campos,[26] A. Carnero Rosell,[27, 23, 28] M. Carrasco Kind,[29, 30] R. Cawthon,[25] R. Chen,[20] P. Chintalapati,[31]
C. Davis,[12] E. Di Valentino,[32] H. T. Diehl,[31] S. Dodelson,[26, 33] C. Doux,[1] A. Drlica-Wagner,[15, 31, 16] K. Eckert,[1] T. F. Eifler,[2, 34]
F. Elsner,[35] S. Everett,[36] A. Farahi,[18, 37] A. Ferté,[34] P. Fosalba,[5, 6] O. Friedrich,[38] M. Gatti,[1] G. Giannini,[39] D. Gruen,[11, 12, 13]
R. A. Gruendl,[29, 30] I. Harrison,[40, 32] W. G. Hartley,[41] E. M. Huff,[34] D. Huterer,[18] A. Kovacs,[27, 28] P. F. Leget,[12] J. McCullough,[12]
J. Muir,[12] J. Myles,[11, 12, 13] A. Navarro-Alsina,[42] Y. Omori,[15, 16, 12] R. P. Rollins,[32] A. Roodman,[12, 13] R. Rosenfeld,[43, 23]
I. Sevilla-Noarbe,[17] E. Sheldon,[44] T. Shin,[1] A. Troja,[43, 23] I. Tutusaus,[5, 6] T. N. Varga,[45, 46] R. H. Wechsler,[11, 12, 13] B. Yanny,[31]
B. Yin,[26] Y. Zhang,[31] J. Zuntz,[47] T. M. C. Abbott,[48] M. Aguena,[23] S. Allam,[31] J. Annis,[31] D. Bacon,[49] E. Bertin,[50, 51]
D. Brooks,[35] D. L. Burke,[12, 13] J. Carretero,[39] C. Conselice,[32, 52] M. Costanzi,[53, 54, 55] L. N. da Costa,[23, 56] M. E. S. Pereira,[18]
J. De Vicente,[17] J. P. Dietrich,[57] P. Doel,[35] A. E. Evrard,[58, 18] I. Ferrero,[59] B. Flaugher,[31] J. Frieman,[31, 16] J. García-Bellido,[60]
E. Gaztanaga,[5, 6] D. W. Gerdes,[58, 18] T. Giannantonio,[61, 38] J. Gschwend,[23, 56] G. Gutierrez,[31] S. R. Hinton,[62] D. L. Hollowood,[36]
K. Honscheid,[9, 14] D. J. James,[63] T. Jeltema,[36] K. Kuehn,[64, 65] N. Kuropatkin,[31] O. Lahav,[35] M. Lima,[66, 23] H. Lin,[31]
M. A. G. Maia,[23, 56] J. L. Marshall,[67] P. Melchior,[68] F. Menanteau,[29, 30] C. J. Miller,[58, 18] R. Miquel,[69, 39] J. J. Mohr,[57, 45]
R. Morgan,[25] A. Palmese,[31, 16] F. Paz-Chinchón,[29, 61] D. Petravick,[29] A. Pieres,[23, 56] A. A. Plazas Malagón,[68] E. Sanchez,[17]
V. Scarpine,[31] S. Serrano,[5, 6] M. Smith,[70] M. Soares-Santos,[18] E. Suchyta,[71] G. Tarle,[18] D. Thomas,[49] and J. Weller[45, 46]

(DES Collaboration)

[1]*Department of Physics and Astronomy, University of Pennsylvania, Philadelphia, PA 19104, USA*
[2]*Department of Astronomy/Steward Observatory, University of Arizona,
933 North Cherry Avenue, Tucson, AZ 85721-0065, USA*
[3]*Lawrence Berkeley National Laboratory, 1 Cyclotron Road, Berkeley, CA 94720, USA*
[4]*Department of Applied Mathematics and Theoretical Physics, University of Cambridge, Cambridge CB3 0WA, UK*
[5]*Institut d'Estudis Espacials de Catalunya (IEEC), 08034 Barcelona, Spain*
[6]*Institute of Space Sciences (ICE, CSIC), Campus UAB,
Carrer de Can Magrans, s/n, 08193 Barcelona, Spain*
[7]*Department of Physics, Northeastern University, Boston, MA 02115, USA*
[8]*Laboratory of Astrophysics, École Polytechnique Fédérale de Lausanne (EPFL), Observatoire de Sauverny, 1290 Versoix, Switzerland*
[9]*Center for Cosmology and Astro-Particle Physics, The Ohio State University, Columbus, OH 43210, USA*
[10]*Department of Physics, University of Arizona, Tucson, AZ 85721, USA*
[11]*Department of Physics, Stanford University, 382 Via Pueblo Mall, Stanford, CA 94305, USA*
[12]*Kavli Institute for Particle Astrophysics & Cosmology,
P. O. Box 2450, Stanford University, Stanford, CA 94305, USA*
[13]*SLAC National Accelerator Laboratory, Menlo Park, CA 94025, USA*
[14]*Department of Physics, The Ohio State University, Columbus, OH 43210, USA*
[15]*Department of Astronomy and Astrophysics, University of Chicago, Chicago, IL 60637, USA*
[16]*Kavli Institute for Cosmological Physics, University of Chicago, Chicago, IL 60637, USA*
[17]*Centro de Investigaciones Energéticas, Medioambientales y Tecnológicas (CIEMAT), Madrid, Spain*
[18]*Department of Physics, University of Michigan, Ann Arbor, MI 48109, USA*
[19]*Kavli Institute for the Physics and Mathematics of the Universe (WPI),
UTIAS, The University of Tokyo, Kashiwa, Chiba 277-8583, Japan*
[20]*Department of Physics, Duke University Durham, NC 27708, USA*
[21]*Argonne National Laboratory, 9700 South Cass Avenue, Lemont, IL 60439, USA*
[22]*Instituto de Física Teórica, Universidade Estadual Paulista, São Paulo, Brazil*
[23]*Laboratório Interinstitucional de e-Astronomia - LIneA,
Rua Gal. José Cristino 77, Rio de Janeiro, RJ - 20921-400, Brazil*
[24]*Institute for Astronomy, University of Hawai'i, 2680 Woodlawn Drive, Honolulu, HI 96822, USA*
[25]*Physics Department, 2320 Chamberlin Hall, University of Wisconsin-Madison, 1150 University Avenue Madison, WI 53706-1390*
[26]*Department of Physics, Carnegie Mellon University, Pittsburgh, Pennsylvania 15312, USA*
[27]*Instituto de Astrofisica de Canarias, E-38205 La Laguna, Tenerife, Spain*
[28]*Universidad de La Laguna, Dpto. AstrofÃsica, E-38206 La Laguna, Tenerife, Spain*
[29]*Center for Astrophysical Surveys, National Center for Supercomputing Applications, 1205 West Clark St., Urbana, IL 61801, USA*
[30]*Department of Astronomy, University of Illinois at Urbana-Champaign, 1002 W. Green Street, Urbana, IL 61801, USA*
[31]*Fermi National Accelerator Laboratory, P. O. Box 500, Batavia, IL 60510, USA*

[32]*Jodrell Bank Center for Astrophysics, School of Physics and Astronomy,*
University of Manchester, Oxford Road, Manchester, M13 9PL, UK
[33]*NSF AI Planning Institute for Physics of the Future,*
Carnegie Mellon University, Pittsburgh, PA 15213, USA
[34]*Jet Propulsion Laboratory, California Institute of Technology, 4800 Oak Grove Dr., Pasadena, CA 91109, USA*
[35]*Department of Physics & Astronomy, University College London, Gower Street, London, WC1E 6BT, UK*
[36]*Santa Cruz Institute for Particle Physics, Santa Cruz, CA 95064, USA*
[37]*Departments of Statistics and Data Science, University of Texas at Austin, Austin, TX 78757, USA*
[38]*Kavli Institute for Cosmology, University of Cambridge, Madingley Road, Cambridge CB3 0HA, UK*
[39]*Institut de Física d'Altes Energies (IFAE), The Barcelona Institute of*
Science and Technology, Campus UAB, 08193 Bellaterra (Barcelona) Spain
[40]*Department of Physics, University of Oxford, Denys Wilkinson Building, Keble Road, Oxford OX1 3RH, UK*
[41]*Department of Astronomy, University of Geneva, ch. d'Écogia 16, CH-1290 Versoix, Switzerland*
[42]*Instituto de Física Gleb Wataghin, Universidade Estadual de Campinas, 13083-859, Campinas, SP, Brazil*
[43]*ICTP South American Institute for Fundamental Research*
Instituto de Física Teórica, Universidade Estadual Paulista, São Paulo, Brazil
[44]*Brookhaven National Laboratory, Bldg 510, Upton, NY 11973, USA*
[45]*Max Planck Institute for Extraterrestrial Physics, Giessenbachstrasse, 85748 Garching, Germany*
[46]*Universitäts-Sternwarte, Fakultät für Physik, Ludwig-Maximilians Universität München, Scheinerstr. 1, 81679 München, Germany*
[47]*Institute for Astronomy, University of Edinburgh, Edinburgh EH9 3HJ, UK*
[48]*Cerro Tololo Inter-American Observatory, NSF's National Optical-Infrared Astronomy Research Laboratory, Casilla 603, La Serena, Chile*
[49]*Institute of Cosmology and Gravitation, University of Portsmouth, Portsmouth, PO1 3FX, UK*
[50]*CNRS, UMR 7095, Institut d'Astrophysique de Paris, F-75014, Paris, France*
[51]*Sorbonne Universités, UPMC Univ Paris 06, UMR 7095,*
Institut d'Astrophysique de Paris, F-75014, Paris, France
[52]*University of Nottingham, School of Physics and Astronomy, Nottingham NG7 2RD, UK*
[53]*Astronomy Unit, Department of Physics, University of Trieste, via Tiepolo 11, I-34131 Trieste, Italy*
[54]*INAF-Osservatorio Astronomico di Trieste, via G. B. Tiepolo 11, I-34143 Trieste, Italy*
[55]*Institute for Fundamental Physics of the Universe, Via Beirut 2, 34014 Trieste, Italy*
[56]*Observatório Nacional, Rua Gal. José Cristino 77, Rio de Janeiro, RJ - 20921-400, Brazil*
[57]*Faculty of Physics, Ludwig-Maximilians-Universität, Scheinerstr. 1, 81679 Munich, Germany*
[58]*Department of Astronomy, University of Michigan, Ann Arbor, MI 48109, USA*
[59]*Institute of Theoretical Astrophysics, University of Oslo. P.O. Box 1029 Blindern, NO-0315 Oslo, Norway*
[60]*Instituto de Fisica Teorica UAM/CSIC, Universidad Autonoma de Madrid, 28049 Madrid, Spain*
[61]*Institute of Astronomy, University of Cambridge, Madingley Road, Cambridge CB3 0HA, UK*
[62]*School of Mathematics and Physics, University of Queensland, Brisbane, QLD 4072, Australia*
[63]*Center for Astrophysics | Harvard & Smithsonian, 60 Garden Street, Cambridge, MA 02138, USA*
[64]*Australian Astronomical Optics, Macquarie University, North Ryde, NSW 2113, Australia*
[65]*Lowell Observatory, 1400 Mars Hill Rd, Flagstaff, AZ 86001, USA*
[66]*Departamento de Física Matemática, Instituto de Física,*
Universidade de São Paulo, CP 66318, São Paulo, SP, 05314-970, Brazil
[67]*George P. and Cynthia Woods Mitchell Institute for Fundamental Physics and Astronomy,*
and Department of Physics and Astronomy, Texas A&M University, College Station, TX 77843, USA
[68]*Department of Astrophysical Sciences, Princeton University, Peyton Hall, Princeton, NJ 08544, USA*
[69]*Institució Catalana de Recerca i Estudis Avançats, E-08010 Barcelona, Spain*
[70]*School of Physics and Astronomy, University of Southampton, Southampton, SO17 1BJ, UK*
[71]*Computer Science and Mathematics Division, Oak Ridge National Laboratory, Oak Ridge, TN 37831*

We constrain cosmological parameters and galaxy-bias parameters using the combination of galaxy clustering and galaxy-galaxy lensing measurements from the Dark Energy Survey Year-3 data. We describe our modeling framework and choice of scales analyzed, validating their robustness to theoretical uncertainties in small-scale clustering by analyzing simulated data. Using a linear galaxy bias model and `redMaGiC` galaxy sample, we obtain constraints on the matter content of the universe to be $\Omega_m = 0.325^{+0.033}_{-0.034}$. We also implement a non-linear galaxy bias model to probe smaller scales that includes parameterizations based on hybrid perturbation theory, and find that it leads to a 17% gain in cosmological constraining power. Using the `redMaGiC` galaxy sample as foreground lens galaxies, we find the galaxy clustering and galaxy-galaxy lensing measurements to exhibit significant signals akin to decorrelation between galaxies and mass on large scales, which is not expected in any current models. This likely systematic measurement error biases our constraints on galaxy bias and the S_8 parameter. We find that a scale-, redshift- and sky-area-independent phenomenological decorrelation parameter can effectively capture this inconsistency between the galaxy clustering and galaxy-galaxy lensing. We perform robustness tests of our methodology pipeline and demonstrate stability of the constraints to changes in the theory model. After accounting for this decorrelation, we infer the constraints on the mean host halo mass of the `redMaGiC` galaxies from the large-scale bias constraints, finding the galaxies occupy halos of mass approximately $1.5 \times 10^{13} M_\odot/h$.

I. INTRODUCTION

Wide-area imaging surveys of galaxies provide cosmological information through measurements of galaxy clustering and weak gravitational lensing. Galaxies are useful tracers of the full matter distribution, and their spatial clustering is used to infer the matter power spectrum. The shapes of distant galaxies are lensed by the intervening matter, providing a second way to probe the mass distribution. With wide-area galaxy surveys, these two probes of the late time universe have provided information on both the geometry and growth of structure in the universe. In recent years, the combination of three two-point correlations—cosmic shear (the lensing shear auto-correlation), galaxy-galaxy lensing (the cross-correlation of lens galaxy positions with shear) and the angular auto-correlation of the lens galaxy positions—have been developed in a theoretical framework [6, 13, 14, 115, 123] and used to constrain cosmological parameters [15, 20, 30, 66, 80, 82, 104, 116]. In practice, two galaxy samples are used: *lens* galaxies tracing the foreground large scale structure, and background *source* galaxies whose shapes are used to infer the lensing shear. The Dark Energy Survey (DES) presented cosmological constraints from their Year 1 (Y1) data set from cosmic shear [111] and a joint analysis of all three two-point correlations (henceforth called the "3×2pt" datavector) [1].

This paper is part of a series describing the methodology and results of DES Year 3 (Y3) 3×2pt analysis. The cosmological constraints are presented for cosmic shear [5, 99], the combination of galaxy clustering and galaxy-galaxy lensing using two different lens galaxy samples [this paper; 31, 89], as well as the 3×2pt analysis [23]. These cosmological results are enabled by extensive methodology developments at all stages of the analysis from pixels to cosmology, which are referenced throughout. This paper presents the modeling methodology and cosmology inference from DES Y3 galaxy clustering [93] and galaxy-galaxy lensing [92] measurements. We focus on the `redMaGiC` [94] galaxy sample, described further below. A parallel analysis using a different galaxy sample, the `MagLim` sample [90], is presented in a separate paper [89].

Incomplete theoretical understanding of the relationship of galaxies to the mass distribution, called galaxy bias, has been a limiting factor in interpreting the lens galaxy auto-correlation function (denoted $w(\theta)$) and galaxy-galaxy lensing (and denoted $\gamma_t(\theta)$). At large scales, galaxy bias can be described by a single number, the linear bias b_1. On smaller scales, bias is non-local and non-linear, and its description is complicated [43, 98]. Perturbation theory (PT) approaches have been developed for quasi-linear scales ~ 10 Mpc, though the precise range of scales of its validity is a subtle question that depends on the galaxy population, the theoretical model, and the statistical power of the survey.

With a model for galaxy bias, $w(\theta)$ and γ_t measurements, together called the "2×2pt" datavector, can probe the underlying matter power spectrum. They are also sensitive to the

distance-redshift relation over the redshift range of the lens and source galaxy distributions. These two datavectors constitute a useful subset of the full 3×2pt datavector, since bias and cosmological parameters can both be constrained (though the uncertainty in galaxy bias would limit either $w(\theta)$ or $\gamma_t(\theta)$ individually).

A major part of the modeling and validation involves PT models of galaxy bias and tests using mock catalogs based on N-body simulations with various schemes of populating galaxies. Approaches based on the halo occupation distribution (HOD) have been widely developed and are used for the DES galaxy samples. For the Year 3 (Y3) dataset of DES, two independent sets of mock catalogs have been developed, based on the `Buzzard`[25] and `MICE` simulations [22, 40, 41].

An interesting recent development in cosmology is a possible disagreement between the inference of the expansion rate and the amplitude of mass fluctuations (denoted σ_8) and direct measurements or the inference of these quantities in the late-time universe. The predictions are anchored via measurements of the cosmic microwave background (CMB) and use general relativity and a cosmological model of the universe to extrapolate to late times. This cosmological model, denoted by ΛCDM, relies on two ingredients in the energy budget of the universe that have yet to be directly detected: cold dark matter (CDM) and dark energy in the form of a cosmological constant denoted as Λ. The value of σ_8 inferred from measurements of cosmic shear and the 3×2pt datavector [1, 5, 23, 51, 52, 99, 111], from galaxy clusters [2, 110] and the redshift-space power spectrum [88] tends to be lower than the CMB prediction. The significance of this tension is a work in progress and crucial to the viability of ΛCDM. The Hubble tension refers to the measured expansion rate being higher than predicted by the CMB. The resolution of the two tensions, and their possible relationship, is an active area of research in cosmology and provides additional context for the analysis presented here.

Figure 1, based on simulated data, shows the expected constraints on S_8 and Ω_m from the 2×2pt datavector and cosmic shear (1×2pt). It is evident that the two have some complementarity, which enables the breaking of degeneracies in both ΛCDM and wCDM cosmological models (where w is the dark energy equation of state parameter and $w \neq -1$ points towards the departure from standard ΛCDM model). Particularly noteworthy are the significantly better constraints compared to 1×2pt on the parameter w and Ω_m using 2×2pt in the wCDM and ΛCDM models respectively. Note that unlike in 1×2pt, where all the matter in front of source galaxy contributes to its signal, 2×2pt receives contribution only from galaxies within the narrow lens redshift bins. Therefore, we attribute better constraints on these cosmological parameters from 2×2pt to significantly more precise redshifts of the lens galaxy sample. This allows for precise tomographic measurements of 2×2pt datavector which constrains the background geometric parameters like w and Ω_m. With data, these somewhat independent avenues to cosmology provide a valuable cross-check, as the leading sources of systematics are largely different.

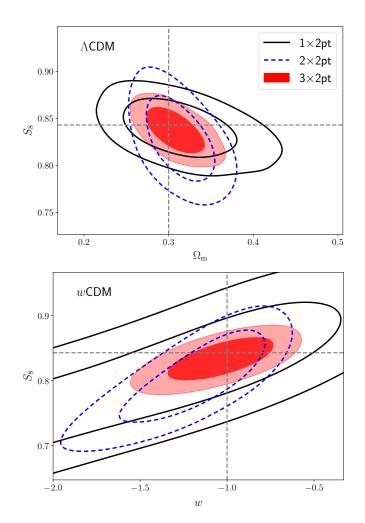The formalism used to compute the 2×2pt datavector is

* shivamp@sas.upenn.edu

Figure 1. Comparison of *simulated* constraints on cosmological parameters Ω_m and S_8 from cosmic shear alone (1×2pt), galaxy clustering + galaxy-galaxy lensing (2×2pt) and including all three probes (3×2pt). This plot uses a *simulated noise-less baseline datavector* (see §IV B) and shows that 2×2pt adds complementary information to cosmic shear constraints, particularly, providing stronger constraints on Ω_m and w.

presented in §II. The description of the lens and source galaxy samples, their redshift distributions and measurement methodology of our datavector and its covariance estimation are presented in §III. In §IV we validate our methodology using N-body simulations and determine the scale cuts for our analysis. Note that in this paper we focus on validation of analysis when using the `redMaGiC` lens galaxy sample and we refer the reader to Porredon et al. [89] for validation of analysis choices for the `MagLim` sample. The results on data are presented in §V, and we conclude in §VI.

II. THEORETICAL MODEL

A. Two-point correlations

Here we describe the hybrid perturbation theory (PT) model used to make theoretical predictions for the two-point statistics $w(\theta)$ and $\gamma_t(\theta)$.

1. Power spectrum

To compute the two-point projected statistics $w(\theta)$ and $\gamma_t(\theta)$, we first describe our methodology of predicting galaxy-galaxy and galaxy-matter power spectra (P_{gg} and P_{gm} respectively). PT provides a framework to describe the distribution of biased tracers of the underlying dark matter field in quasi-linear and linear scales. This framework allows for an order-by-order controlled expansion of the overdensity of biased tracer (here galaxies) in terms of the overdensity of the dark matter field where successively higher-order non-linearities dominate only in successively smaller-scale modes. We will analyze two PT models in this analysis, an effective linear bias model (that is complete only at first order) and an effective one–loop PT model (that is complete up-to third order).

For the linear bias model, we can write the galaxy-matter cross spectrum as $P_{gm}(k) = b_1 P_{mm}$ and auto-power spectrum of the galaxies as $P_{gg}(k) = b_1^2 P_{mm}(k)$. Here b_1 is the linear bias parameter and $P_{mm}(k)$ is the *non-linear* power spectrum of the matter field. We use the non-linear matter power spectrum prediction from Takahashi et al. [107] to model $P_{mm}(k)$ (referred to as HALOFIT hereafter). We use the Bird et al. [9] prescription to model the impact of massive neutrinos in this HALOFIT fitting formula. See [64] for robustness tests of this choice.

In the effective one–loop PT model used here, P_{gm} and P_{gg} can be expressed as:

$$P_{gm}(k, z) = b_1 P_{mm}(k, z) + \frac{1}{2} b_2 P_{b_1 b_2}(k, z) + \frac{1}{2} b_s P_{b_1 s^2}(k, z)$$
$$+ \frac{1}{2} b_{3nl} P_{b_1 b_{3nl}}(k, z) \tag{1}$$
$$P_{gg}(k, z) = b_1^2 P_{mm}(k, z) + b_1 b_2 P_{b_1 b_2}(k, z) + b_1 b_s P_{b_1 s^2}(k, z)$$
$$+ b_1 b_{3nl} P_{b_1 b_{3nl}}(k, z) + \frac{1}{4} b_2^2 P_{b_2 b_2}(k, z)$$
$$+ \frac{1}{2} b_2 b_s P_{b_2 s^2}(k, z) + \frac{1}{4} b_s^2 P_{s^2 s^2}(k, z). \tag{2}$$

Here the parameters b_1, b_2, b_s and b_{3nl} are the renormalized bias parameters [81]. The kernels $P_{b_1 b_2}$, $P_{b_1 s^2}$, $P_{b_1 b_{3nl}}$, $P_{b_2 b_2}$, $P_{b_2 s^2}$ and $P_{s^2 s^2}$ are described in [95] and are calculable from the linear matter power spectrum. We validated this model in [87] using 3D correlation functions, ξ_{gg} and ξ_{gm}, of `redMaGiC` galaxies measured in DES-like simulations. These configuration space statistics are the Fourier transforms of the power spectra mentioned above. We found this model to describe the high signal-to-noise 3D measurements above scales of 4 Mpc/h and redshift $z < 1$ with a reduced χ^2 consistent with one. Our

tests also showed that at the projected precision of this analysis, two of the nonlinear bias parameters (b_s and b_{3nl}) can be fixed to their co-evolution values given by $b_s = (-4/7)(b_1 - 1)$ and $b_{3nl} = (b_1 - 1)$. We will use this result as our *fiducial* modeling choice for the one–loop PT model.

2. Angular correlations

In order to calculate our observables $w(\theta)$ and $\gamma_t(\theta)$, we project the 3D power spectra described above to angular space. The projected galaxy clustering and galaxy-galaxy lensing angular power spectra of tomography bins i, j are given by:

$$C_{AB}^{ij}(\ell) = \frac{2}{\pi} \int d\chi_1 W_A^i(\chi_1) \int d\chi_2 W_B^j(\chi_2)$$
$$\int dk \, k^2 \, P_{AB}(k, z(\chi_1), z(\chi_2)) j_\ell(k\chi_1) j_\ell(k\chi_2), \tag{3}$$

where, $AB = gg$ models galaxy clustering and $AB = g\kappa$, where κ denotes the convergence field, models galaxy-galaxy lensing. Here $W_g^i(\chi) = n_g^i(z(\chi)) dz/d\chi$ is the normalized radial selection function of lens galaxies for tomographic bin i, and W_κ^i is the tomographic lensing efficiency of the source sample

$$W_\kappa^i(\chi) = \frac{3\Omega_m H_0^2}{2} \int_\chi^\infty d\chi' n_s'(z(\chi')) \frac{\chi}{a(\chi)} \frac{\chi' - \chi}{\chi'}, \tag{4}$$

with $n_{g/s}^i(z)$ the normalized redshift distribution of the lens/source galaxies in tomography bin i. For the galaxy-galaxy lensing observable, we use the Limber approximation [76, 77] which simplifies the Eq. 3 to

$$C_{g\kappa}^{ij}(\ell) = \int d\chi \frac{W_g^i(\chi) W_\kappa^j(\chi)}{\chi^2} P_{g\kappa}\left(k = \frac{l + 1/2}{\chi}, z(\chi)\right). \tag{5}$$

In the absence of other modeling ingredients that are described in the next section, we have $C_{g\kappa}^{ij}(\ell) \equiv C_{gm}^{ij}(\ell)$ (similarly $P_{g\kappa} \equiv P_{gm}$). As described in Fang et al. [35], even at the accuracy beyond this analysis, it is sufficient to use the Limber approximation for the galaxy-galaxy lensing observable, while for galaxy clustering this may cause significant cosmological parameter biases.

To evaluate galaxy clustering statistics using Eq. 3, we split the predictions into small and large scales. The non-Limber correction is only significant on large scales where non-linear contributions to the matter power spectra as well as galaxy biasing are sub-dominant. Therefore we use the Limber approximation for the small-scale non-linear corrections and use non-Limber corrections strictly on large scales using linear theory. Schematically, i.e., ignoring contributions from redshift-space distortions and lens magnification [see 64, for details], the galaxy clustering angular power spectrum between tomographic bins i and j is given by:

$$C_{gg}^{ij}(\ell)$$
$$= \int d\chi \frac{W_g^i(\chi) W_g^j(\chi)}{\chi^2} \left[P_{gg}\left(\frac{\ell + 0.5}{\chi}, \chi\right) - b_1^i b_1^j P_{lin}\left(\frac{\ell + 0.5}{\chi}, \chi\right) \right]$$
$$+ \frac{2}{\pi} \int d\chi_1 b_1^i W_g^i(\chi_1) D(z(\chi_1)) \int d\chi_2 b_1^j W_g^j(\chi_2) D(z(\chi_2)) \int \frac{dk}{k} k^3 P_{lin}(k, 0) j_\ell(k\chi_1) j_\ell(k\chi_2), \tag{6}$$

where $D(z(\chi))$ is the growth factor, and P_{lin} is the linear matter power spectrum. The full model of galaxy clustering, including the contributions from other modeling ingredients like redshift-space distortions and lens magnification that we describe below, is detailed in [35] and [64].

The real-space projected statistics of interest can be obtained from these angular correlations via:

$$w^{ij}(\theta) = \sum \frac{2\ell + 1}{4\pi} \overline{P_\ell}(\cos(\theta)) \, C_{gg}^{ij}(\ell) \tag{7}$$

$$\gamma_t^{ij}(\theta) = \sum \frac{2\ell + 1}{4\pi\ell(\ell + 1)} \overline{P_\ell^2}(\cos(\theta)) \, C_{g\kappa}^{ij}(\ell) \tag{8}$$

where $\overline{P_\ell}$ and $\overline{P_\ell^2}$ are bin-averaged Legendre Polynomials (see [42] for exact expressions).

B. The rest of the model

To describe the statistics measured from data, we have to model various other physical phenomena that contribute to the signal to obtain unbiased inferences. In this section, we describe the leading sources of these modeling systematics. We have also validated in [64] that higher-order corrections do not bias our results.

1. Intrinsic Alignment

Galaxy-galaxy lensing aims to isolate the percent-level coherent shape distortions, or shear, of background source galaxies due to the gravitational potential of foreground lens galaxies. The local environment, however, including the gravitational tidal field, can also impact the intrinsic shapes of source

galaxies and contribute to the measured shear signal. This interaction between the source galaxies and their local environment, generally known as "intrinsic alignments" (IA) is non-random. When there is a non-zero overlap between the source and lens redshift distributions, IA can have a non-zero contribution to the galaxy-galaxy lensing signal. To account for this effect, we model IAs using the "tidal alignment and tidal torquing" (TATT) model [11]. Ignoring higher-order effects, such as lens magnification (see [31, 92]), IA contributes to the galaxy-shear angular power spectra through the correlation of lens density and the E-mode component of intrinsic source shapes: $C_{g\kappa}^{ij}(\ell) \to C_{g\kappa}^{ij}(\ell) + C_{gI_E}^{ij}(\ell)$. The $C_{gI_E}^{ij}(\ell)$ term is detailed in Krause et al. [64], Secco, Samuroff et al. [99], Prat et al. [92], and Blazek et al. [11]. Within our implementation of the TATT framework, $C_{gI_E}^{ij}(\ell)$ for all tomographic bin combinations i and j can be expressed using five IA parameters — a_1 and a_2 (normalization of linear and quadratic alignments); α_1 and α_2 (their respective redshift evolution); and b_{ta} (normalization of a density-weighting term) — and the linear lens galaxy bias. Therefore this model captures higher order contributions to the intrinsic alignment of source galaxies as compared to the simpler non-linear alignment (NLA) model that was used in the DES Y1 analysis [1, 63]. In principle, there are also contributions at one-loop order in PT involving the non-linear galaxy bias and non-linear IA terms. However, in this analysis, we neglect these terms as we expect them to be subdominant, and they can be largely captured through the free b_{ta} parameter (see [10] for further discussion of these terms).

2. Magnification

All the matter between the observed galaxy and the observer acts as a gravitational lens. Hence, the galaxies get magnified, increasing the size of galaxy images (parameterized by the magnification factor, μ) and increasing their total flux. The galaxy magnification decreases the observed number density due to stretching of the local sky, whereas increasing the total flux results in an increase in number density (as intrinsically fainter galaxies, which are more numerous, can be observed). This changes the galaxy-galaxy angular power spectrum to: $C_{gg}^{ij}(\ell) \to C_{gg}^{ij}(\ell) + C_{\mu g}^{ij}(\ell) + C_{\mu\mu}^{ij}(\ell)$ and the galaxy-shear angular power spectrum to $C_{g\kappa}^{ij}(\ell) \to C_{g\kappa}^{ij}(\ell) + C_{\mu I_E}^{ij}(\ell) + C_{\mu\kappa}^{ij}(\ell)$. The auto and cross-power spectra with magnification are again given by Eq.3 (see [64] for the detailed description of the equations for each of the power spectra).

The magnification coefficients are computed with the BALROG image simulations [32, 106] in a process described in [31]. Galaxy profiles are drawn from the DES deep fields [50] and injected into real DES images [83]. The full photometry pipeline [100] and redMaGiC sample selection are applied to the new images to produce a simulated redMaGiC sample with the same selection effects as the real data. To compute the impact of magnification, the process is repeated, this time applying a constant magnification to each injected galaxy. The magnification coefficients are then derived from the fractional increase in number density when magnification is applied.

This method captures both the impact of magnification on the galaxy magnitudes and the galaxy sizes, including all numerous sample selection effects. A similar procedure is repeated to estimate the magnification coefficients for the MagLim sample. We refer the reader to Elvin-Poole, MacCrann et al. [31] for further details about the impact of magnification on our observable and their constraints from data.

3. Non-locality of galaxy-galaxy lensing

The configuration-space estimate of the galaxy-galaxy lensing signal is a non-local statistic. The galaxy-galaxy lensing signal of source galaxy at redshift z_s by the matter around galaxy at redshift z_l at transverse distance R is related to the mass density of matter around lens galaxy by:

$$\gamma_t(R; z_g, z_s) = \frac{\Delta\Sigma(R; z_g)}{\Sigma_{\rm crit}(z_g, z_s)}, \qquad (9)$$

where, $\Delta\Sigma(R; z_g) = \bar{\Sigma}(0, R; z_g) - \Sigma(R; z_g)$ and $\Sigma(R; z_g)$ is the surface mass density at a transverse separation R from the lens and $\bar{\Sigma}(0, R)$ is the average surface mass density within a separation R from that lens. Through the $\bar{\Sigma}(0, R)$ term, γ_t at any scale R is dependent on the mass distribution at all scales less than R. This makes γ_t highly non-local, and any model that is valid only on large scales above some $r_{\min}$ will break down more rapidly than for a more local statistic like $w(\theta)$. However, as the dependence on small scales is through the *mean* surface mass density, the impact of the mass distribution inside $r_{\min}$ on $\gamma_t(\theta)$ can be written as:

$$\gamma_t(R; z_g, z_s) = \frac{1}{\Sigma_{\rm crit}(z_g, z_s)}\left(\Delta\Sigma_{\rm model}(z_g) + \frac{B(z_g)}{R^2}\right), \quad (10)$$

where $\Delta\Sigma^{\rm model}$ is the prediction from a model (which is given by PT here) that is valid on scales above $r_{\min}$ (also see [6]). Here, B is the effective total residual mass below $r_{\min}$ and is known as the point mass (PM) parameter. In this analysis we use the thin redshift bin approximation (see Appendix A for details of this validation) and hence the average γ_t signal between lens bin i and source bin j can be written as:

$$\gamma_t^{ij} = \gamma_{t,{\rm model}}^{ij} + G^{ij}/\theta^2, \qquad (11)$$

where,

$$G^{ij} = B^i \int dz_g\, dz_s\, n_g^i\, n_s^j\, \Sigma_{\rm crit}^{-1}(z_g, z_s)\, \chi^{-2}(z_g) \equiv B^i\, \beta^{ij}\,. \qquad (12)$$

Here B^i is the PM for lens bin i, n_g^i is the redshift distribution of lens galaxies for tomographic bin i, n_s^j is the redshift distribution of source galaxies for tomographic bin j.

However, instead of directly sampling over the parameters B^i for each tomographic bin, we implement an analytic marginalization scheme as described in [79]. We modify our inverse-covariance when calculating the likelihood as described in §III D 2.

III. DATA DESCRIPTION

A. DES Y3

The full DES survey was completed in 2019 using the Cerro Tololo Inter-American Observatory (CTIO) 4-m Blanco telescope in Chile and covered approximately 5000 square degrees of the South Galactic Cap. This 570-megapixel Dark Energy Camera [39] images the field in five broadband filters, $grizY$, which span the wavelength range from approximately 400nm to 1060nm. The raw images are processed by the DES Data Management team [84, 101] and after a detailed object selection criteria on the first three years of imaging data (detailed in Abbott & Abdalla et al., [1]), the Y3 GOLD data set containing 400 million sources is constructed (single-epoch and coadd images are available[1] as Data Release 1). We further process this GOLD data set to obtain the lens and source catalogs described in the following sub-sections.

1. redMaGiC lens galaxy sample

The principal lens sample used in this analysis is selected with the redMaGiC algorithm [94] run on DES Year 3 data. redMaGiC selects Luminous Red Galaxies (LRGs) according to the magnitude-color-redshift relation of red-sequence galaxies, calibrated using an overlapping spectroscopic sample. This sample has a threshold luminosity L_{min} and constant co-moving density. The full redMaGiC algorithm is described in Rozo et al. [94], and after application of this algorithm to DES Y3 data, we have approximately 2.6 million galaxies.

Rodríguez-Monroy et al. [93] found that the redMaGiC number density fluctuates with several observational properties of the survey, which imprints a non-cosmological bias into the galaxy clustering. To account for this we assign a weight to each galaxy, which corresponds to the inverse of the angular selection function at that galaxy's location. The computation and validation of these weights are described in [93].

2. MagLim lens galaxy sample

DES cosmological constraints are also derived using a second lens sample, MagLim, selected by applying the criterion $i < 4z + 18$ to the GOLD catalog, where z is the photometric redshift estimate given by DNF [24]. This selection is shown by Porredon et al. [90] to be optimal in terms of its 2×2pt cosmological constraints. We additionally apply a lower magnitude cut, $i > 17.5$, to remove contamination from bright objects. The resulting sample has about 10.7 million galaxies.

Similarly to redMaGiC, we correct the impact of observational systematics on the MagLim galaxy clustering by assigning a weight to each galaxy, as described and validated in

[93]. This sample is then used in Porredon et al. [89] to obtain cosmological constraints from the combination of galaxy clustering and galaxy-galaxy lensing from DES Y3 data. We refer to [89] for a detailed description of the sample and its validation.

3. Source galaxy shape catalog

To estimate the weak lensing shear of the observed source galaxies, we use the METACALIBRATION algorithm [54, 102]. This method estimates the response of a shear estimator to artificially sheared galaxy images and incorporates improvements like better PSF estimation [58], better astrometric methods [100] and inclusion of inverse variance weighting. The details of the method applied to our galaxy sample are presented in [45]. This methodology does not capture the object-blending effects and shear-dependent detection biases and we use image simulations to calibrate this bias as detailed in MacCrann et al. [78]. The galaxies that pass the selection cuts designed to reduce systematic biases (as detailed in Gatti, Sheldon et al. [45]) are used to make our source sample shape catalog. This catalog consists of approximately 100 million galaxies with effective number density of $n_{eff} = 5.6$ galaxies per arcmin^2 and an effective shape noise of $\sigma_e = 0.26$.

B. Buzzard Simulations

The Buzzard simulations are N-body lightcone simulations that have been populated with galaxies using the ADDGALS algorithm [114], endowing each galaxy with positions, velocities, spectral energy distributions, broad-band photometry, half-light radii and ellipticities. In order to build a lightcone that spans the entire redshift range covered by DES Y3 galaxies, we combine three lightcones constructed from simulations with box sizes of 1.05, 2.6 and 4.0 (h^{-3} Gpc^3), mass resolutions of 3.3×10^{10}, 1.6×10^{11}, 5.9×10^{11} $h^{-1}M_\odot$, spanning redshift ranges $0.0 < z \le 0.32$, $0.32 < z \le 0.84$ and $0.84 < z \le 2.35$ respectively. Together these produce $10,000$ square degrees of unique lightcone. The lightcones are run with the L-GADGET2 N-body code, a memory optimized version of GADGET2 [105], with initial conditions generated using 2LPTIC at $z = 50$ [21]. From each $10,000$ square degree catalog, we can create two DES Y3 footprints.

The ADDGALS model uses the relationship, $P(\delta_R|M_r)$, between a local density proxy, δ_R, and absolute magnitude M_r measured from a high-resolution subhalo abundance matching (SHAM) model in order to populate galaxies into these lightcone simulations. The ADDGALS model reproduces the absolute–magnitude–dependent clustering of the SHAM. Additionally, we employ a conditional abundance matching (CAM) model, assigning redder SEDs to galaxies that are closer to massive dark matter halos, in a manner that allows us to reproduce the color-dependent clustering measured in the Sloan Digital Sky Survey Main Galaxy Sample (SDSS MGS) [27, 114].

---

[1] https://des.ncsa.illinois.edu/releases/dr1

These simulations are ray-traced using the spherical-harmonic transform (SHT) configuration of Calclens, where the SHTs are performed on an $N_{\text{side}} = 8192$ HealPix grid [7]. The lensing distortion tensor is computed at each galaxy position and is used to deflect the galaxy angular positions, apply shear to galaxy intrinsic ellipticities, including effects of reduced shear, and magnify galaxy shapes and photometry. We have conducted convergence tests of this algorithm and found that resolution effects are negligible on the scales used for this analysis [25].

Once the simulations have been ray-traced, we apply DES Y3-specific masking and photometric errors. To mask the simulations, we employ the Y3 footprint mask but do not apply the bad region mask [100], resulting in a footprint with an area of 4143.17 square degrees. Each set of three N-body simulations yields two Y3 footprints that contain 520 square degrees of overlap. In total, we use 18 Buzzard realizations in this analysis.

We apply a photometric error model to simulate wide-field photometric errors in our simulations. To select a lens galaxy sample, we run the redMaGiC galaxy selection on our simulations using the same configuration as used in the Y3 data, as described in Rodríguez-Monroy et al. [93]. A weak lensing source selection is applied to the simulations using PSF-convolved sizes and i-band SNR to match the non-tomographic source number density, 5.9 arcmin^{-2}, from the Metacalibration source catalog. This matching was performed using a slightly preliminary version of the Metacalibration catalog, so this number density is slightly different from the final Metacalibration catalog that is used in our DES Y3 analyses. We employ the *fiducial* redshift estimation framework (see §III C 3) to our simulations in order to place galaxies into four source redshift bins with number densities of 1.46 arcmin^{-2} each. Once binned, we match the shape noise of the simulations to that measured in the Metacalibration catalog per tomographic bin, yielding shape noise values of $\sigma_e = [0.247, 0.266, 0.263, 0.314]$.

Two-point functions are measured in the Buzzard simulations using the same pipeline used for the DES Y3 data, where we set Metacalibration responses and inverse variance weights equal to 1 for all galaxies, as these are not assigned in our simulation framework. We have opted to make measurements without shape noise in order to reduce the variance in the simulated analyses using these measurements. Lens galaxy weights are produced in a manner similar to that done in the data and applied to measure our clustering and lensing signals. The clustering and galaxy-galaxy lensing predictions match the DES redMaGiC measurements to $10 - 20\%$ accuracy over most scales and tomographic bins, except for the first lens bin, which disagrees by 50% in $w(\theta)$. We refer the reader to DeRose et al. [26] for a more detailed comparison.

C. Tomography and measurements

1. *redMaGiC redshift methodology*

We split the redMaGiC sample into $N_{\text{z,g}} = 5$ tomographic bins, selected on the redMaGiC redshift point estimate quantity ZREDMAGIC. The bin edges used are $z = 0.15, 0.35, 0.50, 0.65, 0.80, 0.90$. The first three bins use a luminosity threshold of $L_{\text{min}} > 0.5L_*$ and are known as the high-density sample. The last two redshift bins use a luminosity threshold of $L_{\text{min}} > 1.0L_*$ and are known as the high-luminosity sample.

The redshift distributions are computed by stacking four samples from the PDF of each redMaGiC galaxy, allowing for non-Gaussianity of the PDF. We find an average individual redshift uncertainty of $\sigma_z/(1+z) < 0.0126$ in the redshift range used from the variance of these samples. We refer the reader to Rozo et al. [94] for more details on the algorithm of redshift assignment for redMaGiC galaxies and to Cawthon et al. [16] for more details on the calibration of redshift distribution of the Y3 redMaGiC sample.

2. *MagLim redshift methodology*

We use DNF [24] for splitting the MagLim sample into tomographic bins and estimating the redshift distributions. DNF uses a training set from a spectroscopic database as reference, and then provides an estimate of the redshift of the object through a nearest-neighbors fit in a hyperplane in color and magnitude space.

We split the MagLim sample into $N_{\text{z,g}} = 6$ tomographic bins from $z = 0.2$ and $z = 1.05$, selected using the DNF photometric redshift estimate. The bin edges are $[0.20, 0.40, 0.55, 0.70, 0.85, 0.95, 1.05]$. The redshift distributions in each bin are then computed by stacking the DNF PDF estimates of each MagLim galaxy. See [89] for a more comprehensive description and validation of this methodology.

3. *Source redshift methodology*

The description of the tomographic bins of source samples and the methodology for calibrating their photometric redshift distributions are summarized in Myles, Alarcon et al. [85]. Overall, the redshift calibration methodology involves the use of self-organizing maps [85], clustering redshifts [44] and shear-ratio [97] information. The Self-Organizing Map Photometric Redshift (SOMPZ) methodology leverages additional photometric bands in the DES deep-field observations [50] and the Balrog simulation software [33] to characterize a mapping between color space and redshifts. This mapping is then used to provide redshift distribution samples in the wide field, after including the uncertainties from sample variance and galaxy flux measurements in a way that is not subject to selection biases. The clustering redshift methodology performs the calibration by analyzing cross-correlations between
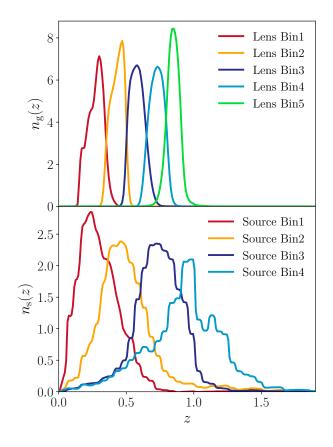
Figure 2. Comparison of the normalized redshift distributions of various tomographic bins of the source galaxies and `redMaGiC` lens galaxies in the data.

`redMaGiC` and spectroscopic data from Baryon Acoustic Oscillation Survey (BOSS) and its extension (eBOSS). Candidate $n_s(z)$ distributions are drawn from the posterior distribution defined by the combination of SOMPZ and clustering-redshift likelihoods. These two approaches provide us the mean redshift distribution of source galaxies and uncertainty in this distribution. The shear-ratio calibration uses the ratios of small-scale galaxy-galaxy lensing data, which are largely independent of the cosmological parameters but help calibrate the uncertainties in the redshift distributions. We include it downstream in our analysis pipeline as an external likelihood, as briefly described in §III C 5 and detailed in Sánchez, Prat et al. [97].

Finally, we split the source catalog into $N_{z,s} = 4$ tomographic bins. The mean redshift distribution of `redMaGiC` lens galaxies and source galaxies are compared in Fig. 2. We refer the reader to Porredon et al. [89] for `MagLim` sample redshift distribution.

4. 2pt measurements

For galaxy clustering, we use the Landy-Szalay estimator [67] given as:

$$w(\theta) = \frac{DD - 2DR + RR}{RR} \tag{13}$$

where DD, DR and RR are normalized weighted number counts of galaxy-galaxy, galaxy-random and random-random pairs within angular and tomographic bins. For lens tomographic bins, we measure the auto-correlations in $N_\theta = 20$ log-spaced angular bins ranging from 2.5 arcmin to 250 arcmin. Each lens galaxy in the catalog (g_i) is weighted with its systematic weight w_{g_i}. This systematic weight aims to remove the large-scale fluctuations due to changing observing conditions at the telescope and Galactic foregrounds. Our catalog of randoms is 40 times larger than the galaxy catalog. The validation of this estimator and systematic weights of the lens galaxies is presented in [93]. In total we have $N_{w(\theta)} = N_{z,g} \times N_\theta = 100$ measured $w(\theta)$ datapoints.

The galaxy-galaxy lensing estimator used in this analysis is given by:

$$\gamma_t(\theta) = \frac{\sum_k w_{r_k}}{\sum_i w_{g_i}} \frac{\sum_{ij} w_{g_i} w_{s_j} e_{t,ij}^{LS}}{\sum_{kj} w_{r_k} w_{s_j}} - \frac{\sum_{kj} w_{r_k} w_{s_j} e_{t,kj}^{RS}}{\sum_{kj} w_{r_k} w_{s_j}} \tag{14}$$

where $e_{t,ij}^{LS}$ and $e_{t,kj}^{RS}$ is the measured tangential ellipticity of source galaxy j around lens galaxy i and random point k respectively. The weight w_{g_i} is the systematic weight of lens galaxy as described above, w_{r_k} is the weight of random point that we fix to 1 and w_{s_j} is the weight of the source galaxy that is computed from inverse variance of the shear response weighted ellipticity of the galaxy (see Gatti, Sheldon et al. [45] for details). This estimator has been detailed and validated in Singh et al. [103] and Prat et al. [92]. We measure this signal for each pair of lens and source tomographic bins and hence in total we have $N_{\gamma_t(\theta)} = N_{z,g} \times N_{z,s} \times N_\theta = 400$ measured $\gamma_t(\theta)$ datapoints.

We analyze both of these measured statistics jointly and hence we have in total $N_{data} = N_{w(\theta)} + N_{\gamma_t(\theta)} = 500$ datapoints. Our measured signal to noise (SNR)^2, using `redMaGiC` lens sample, of $w(\theta)$ is 171 [93], of $\gamma_t(\theta)$ is 121 [92]; giving total joint total SNR of 196. In the §IV, we describe and validate different sets of scale cuts for the linear bias model (angular scales corresponding to (8,6)Mpc/h for $w(\theta)$, $\gamma_t(\theta)$ respectively) and the non-linear bias model ((4,4)Mpc/h). After applying these scale cuts, we obtain the joint SNR, that we analyze for cosmological constraints, as 81 for the linear bias model and 106 for the non-linear bias model.[3]

---

[2] The SNR is calculated as $\sqrt{(\vec{\mathcal{D}} \mathcal{C}^{-1} \vec{\mathcal{D}})}$, where $\vec{\mathcal{D}}$ is the data under consideration and $\mathcal{C}$ is its covariance.

[3] Using a more optimal SNR estimator, SNR= $\frac{(\vec{\mathcal{D}}^{data} \mathcal{C}^{-1} \vec{\mathcal{D}}^{model})}{\sqrt{(\vec{\mathcal{D}}^{model} \mathcal{C}^{-1} \vec{\mathcal{D}}^{model})}}$, where $\vec{\mathcal{D}}^{data}$ is the measured data and $\vec{\mathcal{D}}^{model}$ is the bestfit model, we get SNR=79.5 for the linear bias model scale cuts of (8,6)Mpc/h.

5. Shear ratios

As will be detailed in §IV A 3, in this analysis, we remove the small scales' non-linear information from the 2pt measurements that are presented in the above sub-section. However, as presented in Sánchez, Prat et al. [97], the ratio of $\gamma_t(\theta)$ measurements for the same lens bin but different source bins is well described by our model (see §II) even on small scales. Therefore we include these ratios (referred to as shear-ratio henceforth) as an additional independent dataset in our likelihood. In this shear-ratio datavector, we use the angular scales above 2Mpc/h and less than our *fiducial* scale cuts for 2pt measurements described in §IV A 3 (we also leave two datapoints between 2pt scale cuts and shear-ratio scale cuts to remove any potential correlations between the two). The details of the analysis choices for shear-ratio measurements and the corresponding covariance matrix are detailed in Sánchez, Prat et al. [97] and DES Collaboration [23].

D. Covariance

In this analysis, the covariance between the statistic $w(\theta)$ and $\gamma_t(\theta)$ ($\mathcal{C}$) is modeled as the sum of a Gaussian term ($\mathcal{C}_\mathrm{G}$), trispectrum term ($\mathcal{C}_\mathrm{NG}$) and super-sample covariance term ($\mathcal{C}_\mathrm{SSC}$). The analytic model used to describe ($\mathcal{C}_\mathrm{G}$) is described in [42]. The terms $\mathcal{C}_\mathrm{NG}$ and $\mathcal{C}_\mathrm{SSC}$ are modeled using a halo model framework as detailed in [61, 63]. The covariance calculation has been performed using the CosmoCov package [34], and the robustness of this covariance matrix has been tested and detailed in [42]. We also account for two additional sources of uncertainties that are not included in our *fiducial* model using the methodology of analytical marginalization [12] as detailed below.

1. Accounting for LSS systematics

As described in [93], we modify the $w(\theta)$ covariance to analytically marginalize over two sources of uncertainty in the correction of survey systematics: the choice of correction method, and the bias of the *fiducial* method as measured on simulations.

These systematics are modelled as

$$w'(\theta) = w(\theta) + A_1\Delta w_\mathrm{method}(\theta) + A_2 w_\mathrm{r.\,s.\,bias}(\theta), \quad (15)$$

where $\Delta w_\mathrm{method}(\theta)$ is the difference between two systematics correction methods: Iterative Systematic Decontamination (ISD) and Elastic Net (ENet), and $w_\mathrm{r.\,s.\,bias}(\theta)$ is the residual systematic bias measured on Log-normal mocks. Both terms are presented in detail in [93]. Also note that here A_1 and A_2 are arbitrary amplitudes.

We analytically marginalise over these terms assuming a unit Gaussian as the prior on the amplitudes A_1 and A_2. The measured difference is a 1σ deviation from the prior center. The final additional covariance term to be added to the *fiducial* covariance is:

$$\Delta\mathcal{C} = \Delta\mathbf{w}_\mathrm{method}\Delta\mathbf{w}_\mathrm{method}{}^T + \mathbf{w}_\mathrm{r.\,s.\,bias}\mathbf{w}_\mathrm{r.\,s.\,bias}{}^T. \quad (16)$$

The systematic contribution to each tomographic bin is treated as independent so the covariance between lens bins is not modified.

2. Point mass analytic marginalization

As mentioned in §II B 3, we modify the inverse covariance to perform analytic marginalization over the PM parameters. As detailed in [79], using the generalization of the Sherman-Morrison formula, this procedure changes our *fiducial* inverse-covariance $\mathcal{C}^{-1}$ to $\mathcal{C}_\mathrm{wPM}^{-1}$ as follows:

$$\mathcal{C}_\mathrm{wPM}^{-1} = \mathcal{C}^{-1} - \mathcal{C}^{-1}\mathcal{U}(\mathcal{I} + \mathcal{U}^\mathrm{T}\mathcal{C}^{-1}\mathcal{U})^{-1}\mathcal{U}^\mathrm{T}\mathcal{C}^{-1}. \quad (17)$$

Here $\mathcal{C}^{-1}$ is the inverse of the halo-model covariance as described above, $\mathcal{I}$ is the identity matrix and $\mathcal{U}$ is a $N_\mathrm{data}\times N_\mathrm{z,g}$ matrix where the i-th column is given by $\sigma_{B^i}\vec{t}^i$. Here σ_{B^i} is the standard deviation of the Gaussian prior on point mass parameter B^i and $\vec{t}^i$ is given as:

$$\left(\vec{t}^i\right)_a = \begin{cases} 0 & \text{if } a\text{-th element does not correspond} \\ & \text{to } \gamma_t(\theta) \text{ and if lens-redshift of } a\text{-th} \\ & \text{element} \neq i \\ \beta^{ij}\theta_a^{-2} & \text{otherwise} \end{cases} \quad (18)$$

where the expression for β^{ij} is shown in Eq.12. We evaluate that term at fixed *fiducial* cosmology as given in Table I. In our analysis we put a wide prior on PM parameters B^i by choosing $\sigma_{B^i} = 10000$ which translates to the effective mass residual prior of $10^{17} M_\odot/h$ (see Eq. A1).

IV. VALIDATION OF PARAMETER INFERENCE

We assume the likelihood to be a multivariate Gaussian

$$\ln\mathcal{L}(\vec{\mathcal{D}}|\Theta) = -\frac{1}{2}(\vec{\mathcal{D}} - \vec{\mathcal{T}}(\Theta))^\mathrm{T}\,\mathcal{C}_\mathrm{wPM}^{-1}\,(\vec{\mathcal{D}} - \vec{\mathcal{T}}(\Theta)). \quad (19)$$

Here $\vec{\mathcal{D}}$ is the measured $\gamma_t(\theta)$ and $w(\theta)$ datavector of length N_data (if we use all the angular and tomograhic bins), $\vec{\mathcal{T}}$ is the theoretical prediction for these statistics for the parameter values given by Θ, and $\mathcal{C}_\mathrm{wPM}^{-1}$ is the inverse covariance matrix of shape $N_\mathrm{data} \times N_\mathrm{data}$ (including modifications from the PM marginalization term).

For our analysis we use the POLYCHORD sampler with the settings described in [72]. The samplers probe the posterior ($\mathcal{P}(\Theta|\vec{\mathcal{D}})$) which is given by:

$$\mathcal{P}(\Theta|\vec{\mathcal{D}}) = \frac{\mathcal{L}(\vec{\mathcal{D}}|\Theta)\mathrm{P}(\Theta)}{\mathrm{P}(\vec{\mathcal{D}})} \quad (20)$$

where P(Θ) are the priors on the parameters of our model, described in §IV A 4, and P($\vec{\mathcal{D}}$) is the evidence of data.

To estimate the constraints on the cosmological parameters, we have to marginalize the posterior over all the rest of the multi-dimensional parameter space. We quote the mean and 1σ variance of the marginalized posteriors when quoting the constraints. However, note that these marginalized constraints can be biased if the posterior has significant non-Gaussianities, particularly in the case of broad priors assigned to poorly constrained parameters. The maximum-a-posteriori (MAP) point is not affected by such "projection effects"; therefore, we also show the MAP value in our plots. However, we note that in high-dimensional parameter space with a non-trivial structure, it is difficult to converge on a global maximum of the whole posterior (also see Joachimi et al. [59] and citations therein).

A. Analysis choices

In this subsection, we detail the galaxy bias models that we use, describe the free parameters of our models, and choose priors on those parameters.

1. PT Models

In this analysis, we test two different galaxy bias models:

1. *Linear bias* model: The simplest model to describe the overdensity of galaxies, valid at large scales, assumes it to be linearly biased with respect to the dark matter overdensity (see §II A 1). In this model, for each lens tomographic bin j, the average bias of galaxies is given by a constant free parameter b_1^j.

2. *Non-linear bias* model: To describe the clustering of galaxies at smaller scales robustly, we also implement a one–loop PT model. As described in §II A 1, in general, this model has four free bias parameters for each lens tomographic bin. For each tomographic bin j, we fix three of the non-linear parameters to their co-evolution value given by: $b_s^j = (-4/7)(b_1^j - 1)$ and $b_{3nl}^j = b_1^j - 1$ [81, 95]. Therefore, in our implementation, we have two free parameters for each tomographic bin: linear bias b_1^j and non-linear bias b_2^j. This allows us to probe smaller scales with minimal extra degrees of freedom, obtaining tighter constraints on the cosmological parameters while keeping the biases due to projection effects, as described below, in control.

As we describe below, in order to test the robustness of our model, we analyze the bias in the marginalized constraints on cosmological parameters. However, given asymmetric non-Gaussian degeneracies between the parameters of the model (particularly between cosmological parameters and poorly constrained non-linear bias parameters b_2^j and intrinsic alignment parameters), the marginalized constraints show projection effects. We find that imposing priors on the non-linear bias model parameters in combination with σ_8, as $b_1^j \sigma_8$ and $b_2^j \sigma_8^2$ removes much of the posterior projection effect. As detailed later, these parameters are sampled with flat priors. We emphasize that the flat priors imposed on these non-linear combinations of parameters are non-informative, and our final constraints on b_1^j and b_2^j are significantly tighter than the projection of priors on these parameters.

2. Cosmological Models

We report the constraints on two choices of the cosmological model:

1. Flat ΛCDM : We free six cosmological parameters the total matter density Ω_m, the baryonic density Ω_b, the spectral index n_s, the Hubble parameter h, the amplitude of scalar perturbations A_s and $\Omega_\nu h^2$ (where Ω_ν is the massive neutrino density). We assume a a flat cosmological model, and hence the dark energy density, Ω_Λ, is fixed to be $\Omega_\Lambda = 1 - \Omega_m$.

2. Flat wCDM: In addition to the six parameters listed above, we also free the dark energy equation of state parameter w. Note that this parameter is constant in time and $w = -1$ corresponds to ΛCDM cosmological model.

3. Scale cuts

The complex astrophysics of galaxy formation, evolution, and baryonic processes like feedback from active galactic nuclei (AGN), supernova explosions, and cooling make higher-order non-linear contributions that we do not include in our model. The contribution from these poorly understood effects can exceed our statistical uncertainty on the smallest scales; hence we apply scale cuts chosen so that our PT models give unbiased cosmological constraints.

As mentioned earlier, marginalizing over a multi-dimensional parameter space can lead to biased 2D parameter constraints due to projection effects. To calibrate this effect for each of our models, we first perform an analysis using a *baseline* datavector constructed from the *fiducial* values of that model. We then run our MCMC chain on the *contaminated* datavector that includes higher-order non-linearities, and we measure the bias between the peak of the marginalized *baseline* contours and the peak of the marginalized *contaminated* contours.

From a joint analysis of 3D galaxy-galaxy and galaxy-matter correlation functions at fixed cosmology in simulations [87], we find that the *linear bias* model is a good description above 8Mpc/h while the two-parameter *non-linear bias* model describes the correlations above 4Mpc/h. We convert these physical co-moving distances to angular scale cuts for each tomographic bin and treat them as starting guesses. Then for

each model, we iterate over scale cuts until we find the minimum scales at which the bias between marginalized *baseline* and *contaminated* contours is less than 0.3σ. For the ΛCDM model, we impose this criterion on the $\Omega_{\rm m} - S_8$ projected plane, and for the wCDM model, we impose this criterion on all three 2D plane combinations constructed out of $\Omega_{\rm m}$, S_8 and w. Further validation of these cuts is performed using simulations in IV C and DeRose et al. [26].

4. Priors and Fiducial values

We use non-informative priors on the cosmological parameters to ensure statistically independent constraints on them. Although our constraints on cosmological parameters like the Hubble constant h, spectral index $n_{\rm s}$ and baryon fraction $\Omega_{\rm b}$ are modest compared to surveys like *Planck*, we have verified that our choice of wide priors does not bias the inference on our cosmological parameters of interest, $\Omega_{\rm m}$ and S_8.

When analyzing the *linear bias* model, we use a wide uniform prior on these linear bias parameters, given by $0.5 < b_1^j < 3$. For the *non-linear bias* model, as mentioned above, we sample the parameters $b_1^j\sigma_8$ and $b_2^j\sigma_8^2$. We use uninformative uniform priors on these parameters for each tomographic bin j given by $0.67 < b_1^j\sigma_8 < 3.0$ and $-4.2 < b_2^j\sigma_8^2 < 4.2$. At each point in the parameter space, we calculate σ_8 and retrieve the bias parameters b_1^j and b_2^j from the sampled parameters to get the prediction from the theory model. The *fiducial* values of the linear bias parameters b_1^j used in our simulated likelihood tests are motivated by the recovered bias values in N-body simulations and are summarized in Table I. For the non-linear bias parameters, the *fiducial* values of b_2^j are obtained from the interpolated $b_1 - b_2$ relation extracted from 3D tests in MICE simulations (see Fig. 8 of Pandey & Krause et al., [87]) for the *fiducial* b_1^j for each tomographic bin.

For the intrinsic alignment parameters, we again choose uniform and uninformative priors. As the IA parameters are directly dependent on the source galaxy population, it is challenging to motivate a reasonable choice of prior from other studies. The *fiducial* values of these parameters required for the simulated test are motivated by the Y1 analysis as detailed in [96].

We impose an informative prior for our measurement systematics parameters, lens photo-z shift errors ($\Delta z_{\rm g}^j$), lens photo-z width errors ($\sigma z_{\rm g}^j$), source photo-z shift errors ($\Delta z_{\rm s}^j$) and shear calibration biases (m^j) for various tomographic bins i. The photo-z shift parameter changes the redshift distributions for lenses (g) or sources (s) for any tomographic bin j, used in the theory predictions (see §II) as $n_{\rm g/s}^j(z) \longrightarrow n_{\rm g/s}^j(z - \Delta z_{\rm g/s}^j)$, while the photo-$z$ width results in $n_{\rm g}^j(z) \longrightarrow n_{\rm g}^j(\sigma z_{\rm g}^j[z - \langle z \rangle^j] + \langle z \rangle^j)$, where $\langle z \rangle^j$ is the mean redshift of the tomographic bin j. Lastly, the shear calibration uncertainty modifies the galaxy-galaxy lensing signal prediction between lens bin i and source bin j as $\gamma_{\rm t}^{ij} \longrightarrow (1+m^j)\gamma_{\rm t}^{ij}$.

For the source photo-z, we refer the reader to Myles, Alarcon et al. [85] for the characterization of source redshift distribution, Gatti, Giannini et al. [44] for reducing the uncertainty in these redshift distribution using cross-correlations with spectroscopic galaxies and Cordero, Harrison et al. [19] for a validation of the shift parameterization using a more complete method based on sampling the discrete distribution realizations. For the shear calibration biases, we refer the reader to MacCrann et al. [78] which tests the shape measurement pipeline and determine the shear calibration uncertainty while accounting for effects like blending using state-of-art image simulation suite. For the priors on the lens photo-z shift and lens photo-z width errors, we refer the reader to Cawthon et al. [16], which cross-correlated the DES lens samples with spectroscopic galaxy samples from Sloan Digital Sky Survey to calibrate the photometric redshifts of lenses (also see Porredon et al. [89] and Giannini et al. [46] for further details on `MagLim` redshift calibration).

In this paper we fix the magnification coefficients to the best-fit values described in Elvin-Poole, MacCrann et al. [31], Krause et al. [64], but we refer the reader to Elvin-Poole, MacCrann et al. [31] for details on the impact of varying the magnification coefficients on the cosmological constraints. Note that in our tests to obtain scale cuts for cosmological analysis using simulated datavectors (described below), we remain conservative and fix the shear systematics to their *fiducial* values and analyze the datavectors at the mean source redshift distribution $n_{\rm s}(z)$, as shown in Fig. 2.

Model	Parameter	Prior	Fiducial
	Cosmology		
	$\Omega_{\rm m}$	$\mathcal{U}[0.1, 0.9]$	0.3
	$A_s \times 10^{-9}$	$\mathcal{U}[0.5, 5]$	2.19
	$\Omega_{\rm b}$	$\mathcal{U}[0.03, 0.07]$	0.048
	$n_{\rm s}$	$\mathcal{U}[0.87, 1.06]$	0.97
	h	$\mathcal{U}[0.55, 0.91]$	0.69
	$\Omega_\nu h^2 \times 10^{-4}$	$\mathcal{U}[6.0, 64.4]$	8.3
	Intrinsic Alignment		
	a_1	$\mathcal{U}[-5.0, 5.0]$	0.7
	a_2	$\mathcal{U}[-5.0, 5.0]$	-1.36
	α_1	$\mathcal{U}[-5.0, 5.0]$	-1.7
	α_2	$\mathcal{U}[-5.0, 5.0]$	-2.5
	$b_{\rm ta}$	$\mathcal{U}[0.0, 2.0]$	1.0
Common Parameters	**Lens photo-z**		
	$\Delta z_{\rm g}^1$	$\mathcal{G}[0.006, 0.004]$	0.0
	$\Delta z_{\rm g}^2$	$\mathcal{G}[0.001, 0.003]$	0.0
	$\Delta z_{\rm g}^3$	$\mathcal{G}[0.004, 0.003]$	0.0
	$\Delta z_{\rm g}^4$	$\mathcal{G}[-0.002, 0.005]$	0.0
	$\Delta z_{\rm g}^5$	$\mathcal{G}[-0.007, 0.01]$	0.0
	$\sigma z_{\rm g}^5$	$\mathcal{G}[1.23, 0.054]$	1.0
	Shear Calibration		
	m^1	$\mathcal{G}[-0.0063, 0.0091]$	0.0
	m^2	$\mathcal{G}[-0.0198, 0.0078]$	0.0
	m^3	$\mathcal{G}[-0.0241, 0.0076]$	0.0
	m^4	$\mathcal{G}[-0.0369, 0.0076]$	0.0
	Source photo-z		
	$\Delta z_{\rm s}^1$	$\mathcal{G}[0.0, 0.018]$	0.0
	$\Delta z_{\rm s}^2$	$\mathcal{G}[0.0, 0.015]$	0.0
	$\Delta z_{\rm s}^3$	$\mathcal{G}[0.0, 0.011]$	0.0
	$\Delta z_{\rm s}^4$	$\mathcal{G}[0.0, 0.017]$	0.0
	Point Mass		
	B_i		
	$i \in [1, 5]$	$\mathcal{G}[0.0, 10^4]$	0.0
	Cosmology		
wCDM	w	$\mathcal{U}[-2, -0.33]$	-1.0
	Galaxy Bias		
	b_1^i		
Linear Bias	$i \in [1, 3]$	$\mathcal{U}[0.8, 3.0]$	1.7
	b_1^i		
	$i \in [4, 5]$	$\mathcal{U}[0.8, 3.0]$	2.0
	Galaxy Bias		
	$b_1^i \sigma_8$		
	$i \in [1, 3]$	$\mathcal{U}[0.67, 2.52]$	1.42
	$b_1^i \sigma_8$		
	$i \in [4, 5]$	$\mathcal{U}[0.67, 2.52]$	1.68
Non-linear Bias	$b_2^i \sigma_8^2$		
	$i \in [1, 3]$	$\mathcal{U}[-3.5, 3.5]$	0.16
	$b_2^i \sigma_8^2$		
	$i \in [4, 5]$	$\mathcal{U}[-3.5, 3.5]$	0.35

Table I: The parameters varied in different models, their prior range used ($\mathcal{U}[X, Y] \equiv$ Uniform prior between X and Y; $\mathcal{G}[\mu, \sigma] \equiv$ Gaussian prior with mean μ and standard-deviation σ) in this analysis and the *fiducial* values used for simulated likelihood tests.

B. Simulated Likelihood tests

We perform simulated likelihood tests to validate our choices of scale cuts, galaxy bias model and the cosmological model (including priors and external datasets when relevant). In this analysis we focus on determining and validating the scale cuts using redMaGiC lens galaxy sample and we refer the reader to Porredon et al. [89] for validation using the MagLim lens galaxy sample. We require that the choices adopted return unbiased cosmological parameters. This first step based on the tests on noiseless datavectors in the validation is followed by tests on cosmological simulations.

1. Scale cuts for the linear bias model

Our baseline case assumes linear galaxy bias and no baryonic impact on the matter-matter power spectrum. We use the linear bias values for the five lens bins (in order of increasing redshift) $b_1 = 1.7, 1.7, 1.7, 2.0$, and 2.0. We compare the cosmology constraints from the baseline datavector with a simulated datavector contaminated with contributions from non-linear bias and baryonic physics. For non-linear bias, we use the *fiducial* b_2^j values as described in the previous section and fix the bias parameters b_s^j and $b_{3\rm nl}^j$ to their co-evolution values. To capture the effect of baryons, we use the OWLS-AGN datavector, which is based on hydrodynamical simulations that include the effects of supernovae and AGN feedback, metal-dependent radiative cooling, stellar evolution, and kinematic stellar feedback [69].

Fig. 3 shows the 0.3σ contours when implementing the angular cuts corresponding to (8,6) Mpc/h for $w(\theta)$ and $\gamma_{\rm t}$. The left panel is for ΛCDM, and the right panel for wCDM (only the $w - \Omega_{\rm m}$ plane is shown, but we also verified that the criterion is satisfied in the $\Omega_{\rm m} - S_8$ and $S_8 - w$ planes). The figure shows the peaks of marginalized contaminated and baseline posteriors in 2D planes with blue and red markers respectively. We find that a 0.24σ marginalized contaminated contour intersects the peak of baseline marginalized posterior in ΛCDM model, while same is true for a 0.05σ contour in wCDM model. Therefore, we find that for the linear bias model, (8,6) Mpc/h scale cuts pass the above-mentioned criteria that the distance between the peaks of baseline and contaminated contours is less than 0.3σ.

C. Buzzard simulation tests

Finally, we validate our model with mock catalogs from cosmological simulations for analysis choice combinations that pass the simulated likelihood tests. These tests, and tests of cosmic shear and 3×2-point analyses, are presented in full in DeRose et al. [26], and we summarize the details relevant for 2×2-point analyses here. We use the suite of Y3 Buzzard simulations described above. We again require that our analysis choices return unbiased cosmological parameters. In order to reduce the sample variance, we analyze the mean datavector
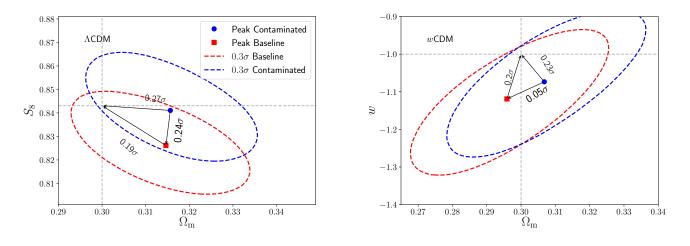
Figure 3. Simulated datavector parameter constraints from a datavector contaminated with non-linear bias + baryons but analyzed with a linear bias + HALOFIT model. Dashed grey lines mark the truth values for the simulated datavector. The left panel shows contours for ΛCDM, and the right panel shows wCDM. The scale cuts are (8,6) Mpc/h for $w(\theta)$ and γ_t respectively. In both panels, we compare the peak of the marginalized constraints in the 2D parameter plane for the contaminated datavector (blue circle) and the baseline datavector (red square). We see that the distance between the peaks of marginalized baseline contours is within 0.3σ of the marginalized contaminated contours, which is our criterion for acceptable scale cuts.

constructed from 18 Buzzard realizations.

1. Validation of linear bias model

We have run simulated 2×2-point analyses on the mean of the measurements from all 18 Buzzard simulations. We compare our model for $w(\theta)$ and $\gamma_t(\theta)$ to our measurements at the true Buzzard cosmology, leaving only linear bias and lens magnification coefficients free. In this case, we have ten free parameters in total, and we find a chi-squared value of 13.6 for 285 data points using our *fiducial* scale cuts and assuming the covariance of a single simulation, as appropriate for application to the data. This analysis assumes true source redshift distributions, and we fix the source redshift uncertainties to zero as a conservative choice. This results in cosmological constraints where the mean two-dimensional parameter biases are 0.23σ in the $S_8 - \Omega_m$ plane and 0.18σ in the $w - \Omega_m$ plane. These biases are consistent with noise, as they have an approximately $1/\sqrt{18}\sigma$ error associated with them (assuming 1σ error from a single realization). We perform a similar analysis using calibrated photometric redshift distributions where we use redMaGiC lens redshift distributions, and use the SOMPZ redshift distribution estimates of source galaxies. These are weighted by the likelihood of those samples given the cross-correlation of our source galaxies with redMaGiC and spectroscopic galaxies (we refer the reader to Appendix F of DeRose et al. [26] for detailed procedure). This procedure results in the mean two-dimensional parameter biases of 0.07σ in the $S_8 - \Omega_m$ plane and 0.05σ in the $w - \Omega_m$ plane.

The left panels of Fig. 4 and Fig. 5 show the 0.3σ constraints obtained from analyzing linear galaxy bias models in ΛCDM

and wCDM cosmologies on the Buzzard datavector in blue colored contours. Since we expect the marginalized posteriors to be affected by the projection effects, we compare these contours to a simulated noiseless baseline datavector obtained at the input cosmology of Buzzard (denoted by gray dashed lines in Fig. 4 and Fig. 5, also see DeRose & Wechsler et al., [25]). We find that similar to results obtained with simulated datavectors in previous section, our parameter biases are less than the threshold of 0.3σ for the fiducial scale cuts. For a more detailed discussion how these shift compare with probability to exceed (PTE) values of exceeding a 0.3σ bias, see Section V of DeRose et al. [26].

Also note that as changing the input truth values of the parameters impacts the shape of the multi-dimensional posterior, we find that the effective magnitude and direction of the projection effects of the baseline contours (comparison of red contours in Fig. 3 with Fig. 4 and Fig. 5) are different.

2. Scale cuts for non-linear bias model

Likewise, we have run simulated 2×2-point analyses including our non-linear bias model on the mean of the measurements from all 18 simulations. Similar to the procedure used to determine the linear bias scale cuts in §IV B 1, we iterate over scale cuts for each tomographic bin defined from varying physical scale cuts.

We compare our model for $w(\theta)$ and $\gamma_t(\theta)$ to our measurements at the true Buzzard cosmology, leaving our bias model parameters and magnification coefficients free, which adds 15 free parameters. We find a χ^2 value of 15.6 for 340 data points using our non-linear bias scale cuts and assuming the

covariance of a single simulation. Simulated analyses using true redshift distributions result in cosmological constraints where the associated mean two-dimensional parameter biases for these analyses are 0.04σ in the $S_8 - \Omega_m$ plane and 0.11σ in the $w - \Omega_m$ plane. This is again consistent with noise due to finite number of realizations.

In the right panel of Figure 4 we show the constraints on Ω_m and S_8 from the mean Buzzard 2×2pt measurements for ΛCDM cosmological model. The results for non-linear bias models are shown, where we find, the criterion for un-biased cosmology is satisfied for the choice of scale cuts of $(4,4)$Mpc/h for $(w(\theta), \gamma_t(\theta))$ respectively. Again for a more detailed discussion how these shift compare with PTE values of exceeding a 0.3σ bias, see DeRose et al. [26]. The Figure 5 shows the same analysis for wCDM cosmological model in the Ω_m and w plane, where we find similar results. We therefore use $(4,4)$Mpc/h as our validated scale cuts when analyzing data with non-linear bias model.

V. RESULTS

In this section we present the 2×2pt cosmology results using the DES Y3 redMaGiC lens galaxy sample and study the implications of our constraints on galaxy bias.

A. redMaGiC cosmology constraints

In Fig. 6, we compare the constraints on the cosmological parameters obtained from jointly analyzing $w(\theta)$ and $\gamma_t(\theta)$ with both linear and non-linear bias models. We find $\Omega_m = 0.325^{+0.033}_{-0.034}$ from the linear bias model (a 10% constraint) at the *fiducial* scale cuts of $(8,6)$ Mpc/h (for $(w(\theta), \gamma_t(\theta))$ respectively), while using the non-linear bias model at same scale cuts gives completely consistent constraints. We also show the results for the scale cuts of $(4,4)$ Mpc/h using the non-linear bias model where we find $\Omega_m = 0.323^{+0.034}_{-0.035}$. These marginalized constraints on Ω_m are completely consistent with the public DES-Y1 2×2pt results [1] and *Planck* results (including all three correlations between temperature and E-mode polarization, see Aghanim et al. [3] for details).

With the analysis of linear bias model with $(8,6)$ Mpc/h scale cuts (referred to as *fiducial* model in following text), we find $S_8 = 0.668^{+0.026}_{-0.033}$. As is evident from the contour plot in Fig. 6, our constraints prefer lower S_8 compared to previous analyses. We use the Monte-Carlo parameter difference distribution methodology (as detailed in Lemos et al. [71]) to assess the tension between our *fiducial* constraints and *Planck* results. Using this criterion, we find a tension of 4.1σ, largely driven by the differences in the S_8 parameter. We find similar constraints on S_8 from the non-linear bias as well for both the scale cuts. We investigate the cause of this low S_8 value in the following sub-sections.

Note that the non-linear bias model at $(4,4)$ Mpc/h scale cuts results in tighter constraints in the $\Omega_m - S_8$ plane. We estimate the total constraining power in this $\Omega_m - S_8$ plane by estimating 2D figure-of-merit (FoM), which is defined as

$\text{FoM}_{p_1,p_2} = 1/\sqrt{(\det \text{Cov}(p_1, p_2))}$, for any two parameters p_1 and p_2 [56, 113]. This statistic here is proportional to the inverse of the confidence region area in the 2D parameter plane of $\Omega_m - S_8$. We find that the non-linear bias model at $(4,4)$ Mpc/h results in a 17% increase in constraining power compared to the linear bias model at $(8,6)$ Mpc/h.

B. Comparison with MagLim results

In Fig. 7, we show the comparison of the cosmology constraints obtained from 2×2pt analysis using the MagLim sample (see Porredon et al. [89]) with the results obtained here with the redMaGiC lens galaxy sample. The top panel compares the $\Omega_m - S_8$ contours assuming ΛCDM cosmology while the bottom panel compares the $\Omega_m - w$ contours assuming wCDM cosmology. We compare both the linear bias and the non-linear bias model at the $(8,6)$ Mpc/h and $(4,4)$ Mpc/h scale cuts respectively. We again find that the S_8 constraints obtained with the redMaGiC sample are low compared to the MagLim sample for both linear and non-linear bias models. As the source galaxy sample, the measurement pipeline and the modeling methodology used are the same for the two 2×2pt analysis, this suggests that the preference for low S_8 in our *fiducial* results is driven by the Y3 redMaGiC lens galaxy sample, which we investigate in the following sub-sections.

In the bottom panel showing the wCDM cosmology constraints, we also show the maximum a posteriori (MAP) estimate in the $\Omega_m - w$ plane, in order to estimate the projection effects arising from marginalizing over the large multi-dimensional space to these two dimensional contours (see Fig. 3 and Fig. 5). We find that the non-linear bias model suffers from mild projection effects (although note the caveats about the MAP estimator mentioned in §IV). We also emphasize that using the non-linear galaxy bias model with smaller scale cuts gives similar improvement in the figure-of-merit of the cosmology contours shown in Fig. 7, using both redMaGiC and MagLim lens galaxy samples.

C. Internal consistency of the redMaGiC results

To investigate the low S_8 constraints in the *fiducial* analysis of the redMaGiC galaxy sample, we first check various aspects of the modeling pipeline. In Fig. 8, we show the constraints on Ω_m, S_8 and galaxy bias for the third tomographic bin b_3, for various robustness tests. We choose to show the third tomographic bin for the galaxy bias constraints as this bin has the highest signal-to-noise ratio. We divide the figure into three parts, separated by horizontal black lines. The bottom panel shows the marginalized constraints from the results described in the previous subsection (see Fig. 6). As mentioned previously, we obtain completely consistent constraints from both linear and non-linear bias models. To check the robustness and keep the interpretation simple, we use the linear bias model using the scale cuts of $(8,6)$ Mpc/h in the following variations.

In the next part of the Figure, moving upwards from the bottom, we test the robustness of the model. In particular,
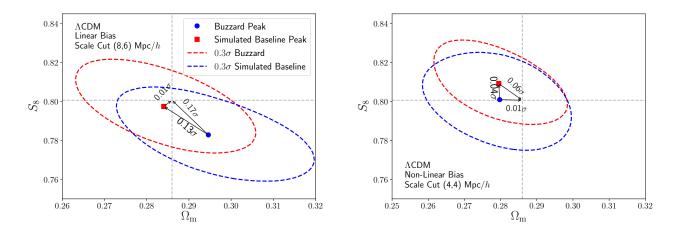
Figure 4. The blue contours show constraints from `Buzzard` simulations (blue contours) compared with `Buzzard` -like theory datavector (red contours) in the ΛCDM cosmological model. The left (right) panel shows the constraints for linear (non-linear) bias models with the scale cuts given in the legend. The linear and non-linear bias values are extracted from fits to the 3D correlation functions (ξ_{gg} and ξ_{gm}). We see that both the scale-cut choices satisfy our validation criterion.
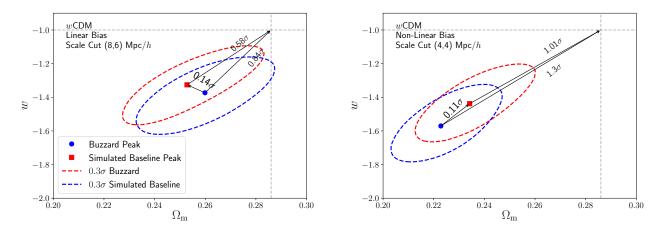
Figure 5. Same as Fig. 4 but for wCDM cosmology.

we check the robustness of the *fiducial* intrinsic alignment model by using the NLA model. We also run the analysis by fixing the neutrino masses to $\Omega_\nu h^2 = 0.00083$. This choice of $\Omega_\nu h^2$ parameter corresponds to the sum of neutrino masses, $\sum m_\nu = 0.06$eV at the *fiducial* cosmology described in Table I (which is the baseline value used in the *Planck* 2018 cosmology results as well [3]). Lastly, we test the impact of varying the dark energy parameter using the wCDM model. We find entirely consistent constraints for all of the above variations.

In the next part of the figure, we test the internal consistency of the datavector. Firstly we remove the contribution of shear-ratio information to the total likelihood, resulting in entirely consistent constraints. Also, note that the size of constraints on the cosmological parameters do not change in this case compared to the *fiducial* results. This demonstrates that the majority of constraints on the cosmological and bias pa-

rameters are obtained from the $w(\theta)$ and $\gamma_t(\theta)$ themselves. We also test the impact of removing one tomographic bin at a time from the datavector. We find consistent constraints in all five cases. Lastly, we also split the datavector into large and small scales. The small-scales run uses the datavector between angular scales corresponding to (8,6) Mpc/h and (30,30) Mpc/h. The large-scales run uses the datavector between angular scales corresponding to (30,30) Mpc/h and 250 arcmins. When analyzing the large scales, we fix the point-mass parameters to their *fiducial* values (see Table I), because of the large degradation of constraining power at these larger-scale cuts due to the degeneracy between point-mass parameters, galaxy bias and cosmological parameter σ_8 (see Appendix A and MacCrann et al. [79]). In both of these cases, we find similar constraints on all parameters, demonstrating that the low S_8 does not originate from either large or small scales.
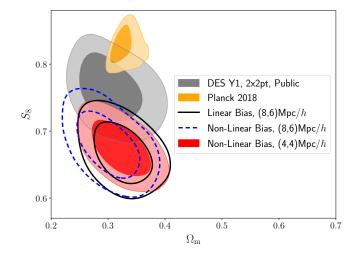
Figure 6. Comparison of the 2×2pt ΛCDM constraints, using `red-MaGiC` lens galaxy sample, for both linear bias and non-linear bias models at their respectively defined scale cuts given in the legend. We find a preference for a low value of S_8, compared to DES Y1 2×2pt public result [1] and Planck 2018 public result [3], with both models of galaxy bias which we investigate in §V C. We also show that analyzing smaller scales using the non-linear galaxy bias model leads to 17% better constraints in the $\Omega_m - S_8$ plane.

As an additional test of the robustness of the modeling pipeline, we analyze the $w(\theta)$ and $\gamma_t(\theta)$ measurements as measured from DES Y1 data [1]. Note that in this analysis, we keep the same scale cuts as described and validated in Abbott et al. [1], which are 8 Mpc/h for $w(\theta)$ and 12 Mpc/h for $\gamma_t(\theta)$. To analyze this datavector, while we use the model described in this paper, we fix the point-mass parameters again to zero due to similar reasons as described above in the analysis of large scales. The constraints we obtain are consistent with the public results described in Abbott et al. [1]. We attribute an approximately 1σ shift in the marginalized Ω_m posterior to the improvements made in the current model, compared to the model used for the public Y1 results [63]. In particular, we use the full non-limber calculation for galaxy clustering and use the TATT model of intrinsic alignment in the model of galaxy-galaxy lensing (also see Fang et al. [35]).

Lastly, to assess the impact of projection effects on the S_8 parameter, we compare the profile posterior to the marginalized posterior. The profile posterior in Fig. 9 is obtained by dividing the samples into 20 bins of S_8 values and calculating the maximum posterior value for each bin. Therefore, unlike the marginalized posterior, the profile posterior does not involve the projection of a high dimensional posterior to a single S_8 parameter. Hence the histogram of the profile posterior is not impacted by projection effects. We compare the marginalized posterior and profile posterior in Fig. 9, demonstrating that projection effects do not impact the inferred S_8 constraints from the marginalized posterior.

In summary, the results presented in this sub-section demonstrate that our modeling methodology is entirely robust, and hence we believe our data are driving the low S_8 constraints with the `redMaGiC` sample. Moreover, as described above, no
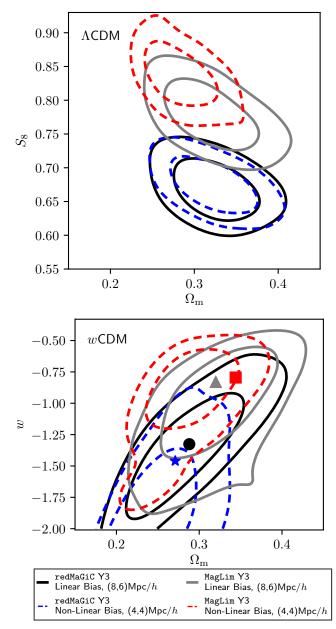
Figure 7. Comparing the constraints from 2×2pt between the `red-MaGiC` and Maglim samples. The black dot and blue star denote the MAP point estimate for `redMaGiC` linear and non-linear bias model respectively, while the gray triangle and red square show the same for the `MagLim` sample.

individual part of the data drives a low value of S_8; therefore, we perform global checks of the datavector in the following sub-sections.

D. Galaxy bias from individual probes

In this sub-section, we test the compatibility of the $w(\theta)$ and $\gamma_t(\theta)$ parts of the datavector. As we will lose the power of complementarity when analyzing them individually, we fix
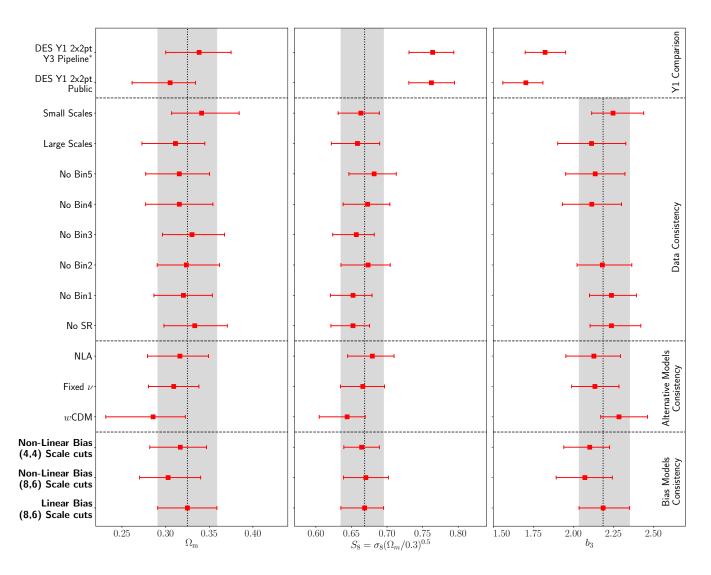
Figure 8. The consistency of the `redMaGiC` 2×2pt cosmology and galaxy bias constraints when changing the analysis choices (see §V C for details). We also compare our constraints to the DES Y1 public 2×2pt results as well as its re-analysis with the current analysis pipeline ($* -$ we fix the point mass parameters when re-analyzing the DES Y1 data due to the large degeneracy between point mass parameters and cosmology at the scale cuts described and validated in Abbott et al. [1]).

the cosmological parameters to the maximum posterior obtained from the DES Y1 3×2pt analysis [1]. We find that the best-fit bias values from the $w(\theta)$ part of the datavector are systematically higher than $\gamma_t(\theta)$ for each tomographic bin. We parameterize this difference in bias values with a phenomenological parameter X for each tomographic bin i as:

$$X^i_{\mathrm{lens}} = b^i_{\gamma_t(\theta)} / b^i_{w(\theta)} \qquad (21)$$

We refer to X as a "decorrelation parameter" because its effect on the data is very similar to assuming that the mass and galaxy density functions have less than 100% correlation. A value of $X = 1$ is expected from local biasing models. The constraints on the parameter X^i_{lens} are shown in Fig. 10. We also compare the constraints of these X^i_{lens} parameters obtained from Y1 `redMaGiC` 2×2pt (see Abbott & Abdalla et al., [1] and Prat & Sánchez et al., [91] for details) and the 2×2pt datavector

using Y3 `MagLim` lens galaxy sample. For the Y1 `redMaGiC` datavector, we fix the scale cuts and priors on the calibration of photometric redshifts of lens and source galaxies as described in the Abbott et al. [1] and for analysis of Y3 `MagLim` datavector we follow the analysis choices detailed in Porredon et al. [89]. In this analysis of all the datavectors, we use the linear bias galaxy bias model while keeping the rest of the model the same as described in §II B. We find that the Y1 `redMaGiC` as well as Y3 `MagLim` 2×2pt data are consistent with $X^i_{\mathrm{lens}} = 1$ for all the tomographic bins, while `redMaGiC` Y3 2×2pt data have a persistent preference for $X^i_{\mathrm{lens}} < 1$ for all the tomographic bins.

Noticeably, we find that for the DES Y1 best-fit cosmological parameters, the Y3 `redMaGiC` datavector prefers a value of $X^i_{\mathrm{lens}} \sim 0.9$ for each tomographic bin. Therefore, in order to keep the interpretation simple, we use a single parameter
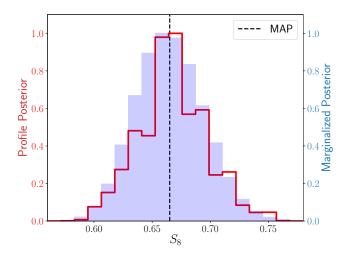
Figure 9. Comparison of the profile posterior and marginalized posterior on the S_8 parameter from the 2×2pt `redMaGiC` LCDM chain.


Figure 10. Constraints on the phenomenological de-correlation parameter, X_{lens}, for each tomographic bin obtained from 2×2pt analysis using Y1 and Y3 `redMaGiC` and Y3 `MagLim` as the lens galaxies (the cosmological parameters are fixed to the DES Y1 best-fit values [1]).
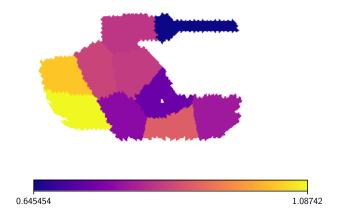
X_{lens} to describe the ratio of galaxy bias $b^i_{\gamma_t(\theta)}/b^i_{w(\theta)}$ for all tomographic bins $i \in [1,5]$. We constrain this single redshift-independent parameter to be $X_{\text{lens}} = 0.9^{+0.03}_{-0.03}$ for Y3 `redMaGiC` , a 3.5σ deviation from $X_{\text{lens}} = 1$. Within general relativity, even when including the impact of non-linear astrophysics, we do not expect a de-correlation between galaxy clustering and galaxy-galaxy lensing to be present at more than a few percent level [28]. We comment on the impact of this de-correlation on the `redMaGiC` cosmology constraints in §V F.

Note that the inferred value of X_{lens} depends on the cosmological parameters, because the large-scale amplitudes of galaxy clustering and galaxy-galaxy lensing involve different combinations of galaxy bias, σ_8 and Ω_m. Therefore, a self-consistent inference of X_{lens} requires the full 3×2pt datavector and is presented in DES Collaboration [23]. However, the DES Y1 3×2pt best-fit cosmological parameters are fairly close to the DES Y3 3×2pt best-fit parameters, therefore we expect the results presented here to be good approximations to those obtained with the Y3 3×2pt datavector.

E. Area split of the de-correlation parameter

In order to further study the properties of this de-correlation parameter X_{lens}, we estimate it independently in 10 approximately equal area patches of the DES Y3 footprint. We measure the datavectors, $w(\theta)$ and $\gamma_t(\theta)$ in each of these 10 patches, using the same methodology presented in §III C 4. In order to obtain the covariance for each patch, we rescale the *fiducial* covariance (see §III D) of the full footprint to the area of each patch. We then estimate X_{lens} from each patch while keeping all the other analysis choices the same.

In Fig. 11 we show the DES footprint split into 10 regions. In this figure, each region is colored in proportion to the mean value of the X_{lens} parameter we obtain using `redMaGiC` as the lens galaxy sample. We run a similar analysis when using `MagLim` as the lens sample.
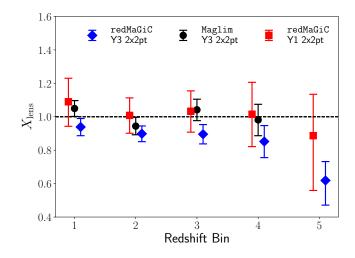
Figure 11. The DES footprint split into 10 regions. The color of each area corresponds to the mean value of the constraints on X_{lens} from that particular area, using the `redMaGiC` lens sample.

In Fig. 12 we show a scatter plot between the value of X_{lens} recovered from each of 10 regions using `redMaGiC` and `MagLim` as lens samples. We find a tight correlation between the value of X_{lens} from the two lens samples. This shows that, compared with `MagLim` , the `redMaGiC` lens sample has a preference for $X_{\text{lens}} < 1$ in the whole DES footprint. Fig. 12 also suggests a large variation in the inferred X_{lens} over the footprint, when compared to `MagLim` . This correlation and area independence of the ratio $X_{\text{Redmagic}}/X_{\text{Maglim}}$ is remarkable and suggests that the potential systematic in the `redMaGiC` sample has a more global origin.

F. Impact of de-correlation on 2×2pt cosmology

To summarize, assuming a standard cosmological model, we have identified that the galaxy-clustering and galaxy-galaxy
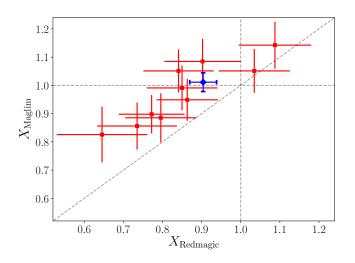
Figure 12. Each red errorbar corresponds to the 68% credible interval constraints on X_{lens} from each of the 10 regions (see Fig. 11), using either `redMaGiC` or `MagLim` lens galaxy sample. The blue errorbar corresponds to the constraints on X_{lens} from the full Y3 area. We find a tight correlation between X_{Redmagic} and X_{Maglim}.
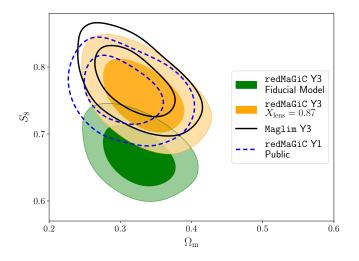

Figure 13. Comparison of the constraints from 2×2pt analysis when using the mean value of X_{lens} parameter for `redMaGiC` lens sample analysis, as estimated and described in DES Collaboration [23]. We find a shift in S_8 parameter compared to our *fiducial* results in §V A, but Ω_{m} constraints are fully consistent.

lensing signal measured using the Y3 `redMaGiC` lens galaxy sample are incompatible with each other (at the set of cosmological parameters preferred by previous studies). We have further identified that this incompatibility is well-captured by a redshift-, scale- and area-independent phenomenological parameter X_{lens}. Using Y3 `redMaGiC` lens sample, we detect $X_{\text{lens}} \sim 0.9$, at the 3.5σ confidence level away from the expected value of $X_{\text{lens}} = 1$. This 2×2pt analysis is done when the cosmological parameters are fixed to their DES Y1 best-fit values; a self-consistent X_{lens} inference analysis with free cosmological parameters requires the full 3×2pt datavector. This is presented in DES Collaboration [23], where the inferred con-

straints on this de-correlation parameter are $X_{\text{lens}} = 0.87^{+0.02}_{-0.02}$.

In Fig. 13, we fix $X_{\text{lens}} = 0.87$ in our model and re-run the Y3 `redMaGiC` 2×2pt analysis. We find, as expected, that this has a significant impact on the marginalized S_8 values and results in the marginalized constraints $S_8 = 0.76^{+0.034}_{-0.037}$, completely consistent with 2×2pt Y1 `redMaGiC` public results as well as Y3 `MagLim` results. Also note that the marginalized constraints on Ω_{m} for $X_{\text{lens}} = 0.87$ model are $\Omega_{\text{m}} = 0.331^{+0.037}_{-0.037}$, which remains consistent with the *fiducial* result.

G. `redMaGiC` host halo mass inference

In the halo model framework (see [18] for a review), the value of the linear bias of a tracer of dark matter can be related to the host halo mass of that tracer. The standard halo occupation distribution (HOD) approach parameterizes the distribution of galaxies inside halos, and hence the observed number density as well as the large scale bias values of any galaxy sample can be expressed in terms of its HOD parameters [8, 119, 120]. The same HOD parameters can also be used to infer the mean host halo mass of the galaxy sample. We use the constraints on linear galaxy bias and the co-moving number density to infer the mean host halo mass of the `red-MaGiC` galaxy sample by marginalizing over HOD parameters. We use the linear bias constraints from the 2×2pt Y3 `red-MaGiC` analysis after fixing $X_{\text{lens}} = 0.87$. This de-correlation parameter results in $w(\theta)$ and γ_{t} preferring different linear bias parameters, related by $b^i(w(\theta))/b^i(\gamma_{\text{t}}(\theta)) = X_{\text{lens}} = 0.87$, for all tomographic bins i. Therefore, we infer the host halo masses using both linear bias parameter values.

The details of the halo model framework used here are given in Appendix C. Note that we have neglected the effects of assembly bias and the correlation between number density and bias constraints in this analysis. With these caveats in mind, in Fig. 14 we show approximately 25% constraints on mean host halo mass of `redMaGiC` galaxies and the constraints for different tomographic bins show its evolution with redshift. This redshift evolution trend is broadly consistent with the pseudo-evolution of halo masses due to changing background reference density with redshift (see [29] for more details). Therefore we find that the DES Y3 `redMaGiC` sample lives in halos of mass of approximately $1.6 \times 10^{13} M_{\odot}/h$, which remains broadly constant with redshift. We find that our results are broadly consistent with the analysis of [17], which used the `redMaGiC` galaxies of DES Science-Verification dataset and estimated the mean halo masses by studying galaxy-galaxy lensing signal in a broad range of scales (including high signal-to-noise small scales that we remove here) using HOD model.[4] We also find broad agreement with a similar study presented in

---

[4] Note that we use M_{200c} as our halo mass definition, which denotes the total mass within a sphere enclosing a mean density which is 200 times the *critical* density of the universe. Clampitt et al. [17] work with M_{200m} as their mass definition, denoting the total mass within a sphere enclosing a mean density which is 200 times the *mean* density of the universe, therefore we convert their constraints to M_{200c} in the above figure.
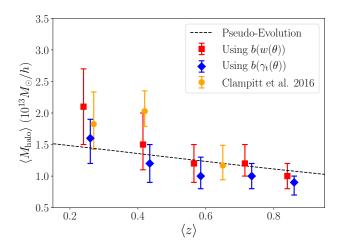
Figure 14. This figure shows the inferred constraints on mean host halo masses of `redMaGiC` galaxies for five tomographic bins. We use the HOD framework to make this inference as detailed in Appendix C and use the bias constraints from a linear bias model 2×2pt chain, fixing $X_{\mathrm{lens}} = 0.87$. We infer the mean host halo masses from the linear bias constraints, $b^i(w(\theta))$ and $b^i(\gamma_{\mathrm{t}}(\theta))$, where they are related as $b^i(w(\theta)/b^i(\gamma_{\mathrm{t}}(\theta) = X_{\mathrm{lens}} = 0.87$ for all the five tomographic bins i. We compare our results to Clampitt et al. [17] and also show the expected pseudo-evolution of a halo having $M_{\mathrm{halo}} = 1.6 \times 10^{13} M_\odot/h$ at $z = 0$.

Zacharegkas, G. et al. [118], analyzing DES Y3 galaxy-galaxy lensing data on a wide range of scales with an improved halo model.

VI. CONCLUSIONS

This paper has presented the cosmological analysis of the $2\times$ 2pt datavector of the DES Year 3 dataset using `redMaGiC` lens sample. We refer the reader to Porredon et al. [89] for similar results using `MagLim` lens sample and Elvin-Poole, MacCrann et al. [31] for details on the impact of lens magnification on the 2×2pt datavector. The 2×2pt datavector comprises the 2-point correlations of galaxy clustering and galaxy lensing using five redshift bins for the lens galaxies and four bins for source galaxies. It provides independent constraints on two primary parameters of interest, the mass density Ω_{m} and amplitude of fluctuations S_8. As shown in Fig. 1, these constraints are complementary to those from cosmic shear. The combination of 2×2pt with cosmic shear is thus better able to constrain Ω_{m}, S_8 as well as the dark energy equation of state parameter w. Perhaps more importantly, this provides a robustness check on the results from either approach.

The estimation and marginalization of galaxy bias parameters is one of the central tasks in extracting cosmology from the 2×2pt datavector. We have developed and validated the methodology for this based on perturbation theory. We use a five-parameter description of galaxy bias per redshift bin, with three of the parameters fixed based on theoretical considerations. We validated these choices using mock catalogs

built on N-body simulations as detailed in our earlier study [87] and Section §IV C. We carry out two analyses: the first using linear bias with more conservative scale cuts, and the second using the full PT bias model going down to smaller scales. Other elements of our model include intrinsic alignments, magnification and "point mass marginalization" (see §II B). The validation of the analysis choice and scale cuts with simulated datavectors (both idealized and from mock catalogs) are presented in §IV A.

Our cosmological results are presented in Figs. 6, 7 and 8, which show preference for low value of S_8 parameter when compared with previous results. We refer the reader to DES Collaboration [23], where, after unblinding the cosmological parameter constraints, we find similar inconsistency in the S_8 parameter constraints between Y3 2×2pt `redMaGiC` analysis and Y3 cosmic shear analysis, as well as a high χ^2 using the ΛCDM model. As detailed in DES Collaboration [23], we discovered that the reason for the high χ^2 of the 3×2pt analysis with the *fiducial* model was due to inconsistencies in the galaxy-galaxy lensing and galaxy clustering signals. The source of this inconsistency is still undetermined, however we found that a single parameter X_{lens}, representing the ratio of the bias inferred from $w(\theta)$ and γ_{t}, substantially improves the goodness of fit. This ratio is cosmology-dependent and can only be inferred consistently (along with the other model parameters) when using the full 3×2pt analysis, presented in DES Collaboration [23].

This ratio is expected to be unity in the absence of galaxy stochasticity, an effect that is expected to be only at the percent level on scales above $\sim 10\,\mathrm{Mpc}$ [28]. Several previous analyses with similar datasets have also found this ratio to be consistent with unity [14, 80, 91]. However, we detect a value of $X_{\mathrm{lens}} = 0.87$, below 1 at the 5-σ level. This purely phenomenological model assumes no scale or redshift dependence, and we found consistent values of X_{lens} when fitting to different scales (see Fig. 8) and when fitting separate values for each *lens* redshift bin (see Fig. 10). Since no known cosmological effect can produce such a large and coherent deviation in clustering and galaxy lensing, we pursued possible systematic errors that could lead to this unusual result. We were unable to verify any such systematics yet, and this is a work in progress. Note that this kind of behavior can arise with potential systematics, for example unaccounted-for impact of photometric uncertainty or background subtraction for large or faint objects on the galaxy selection. This can introduce extra fluctuation of the number density of the lens galaxies across the footprint which will not be captured by the set of survey property maps used in the LSS weights estimation pipeline.

We note that although recent analyses using BOSS galaxies have found similar inconsistencies in the galaxy clustering and galaxy-galaxy lensing (see [68, 70] and references there-in); there are some important differences. In this analysis as well as in DES Collaboration [23], unlike in Leauthaud et al. [70], we do not use any small scale information for galaxy clustering and galaxy-galaxy lensing measurements. Therefore, we are significantly less prone to the impacts of poorly understood small scale non-linear physics, like baryon feedback and galaxy assembly biases [4, 117, 121]. Moreover, in DES

Collaboration [23], by leveraging all the three two-point functions used in 3 × 2pt, the analysis of the consistency between galaxy-lensing and galaxy-clustering can be carried out while freeing the relevant cosmological parameters. The analysis in this paper fixes the cosmological parameters close to the best-fit cosmology from DES Collaboration [23], hence our results are a good approximation to the analysis using the full 3 × 2pt datavector. Similarly, a few recent studies jointly analyzing galaxy clustering auto-correlations and galaxy-CMB lensing cross-correlations have also reported preference for lower galaxy bias value for the cross-correlation compared to the auto correlations [48, 60]. However similar to above analysis with BOSS galaxies, these studies also fix their cosmological parameters to the best-fit cosmology from *Planck* results [3], which is different from this study (see [65] for related discussion).

Fig. 13 shows the 2 × 2pt `redMaGiC` cosmology constraints after fixing $X_{lens} = 0.87$, the best fit value from DES Collaboration [23]. There is a significant shift in S_8, while Ω_m remains stable. Interestingly the resulting contours are fully consistent with the Y1 analysis as well as the 2 × 2pt analysis using the `MagLim` lens galaxy sample [89].

To access the information in the measurements on smaller scales, we use higher-order perturbation theory. We use a hybrid 1-loop perturbation theory model for galaxy bias, capturing the non-linear contributions to the overdensity field till third order. We have tested and validated our model using 3-dimensional correlation functions from DES-mock catalogs in Pandey et al. [87] as well as with projected statistics in DeRose et al. [26]; in this study, we validate the bias model with mocks for the 2 × 2pt `redMaGiC` datavector at scales above 4Mpc/h. This validation presented here, along with results in Pandey et al. [87], are then also directly used to validate non-linear bias model for `MagLim` datavector. We apply it to the data and find that the non-linear bias model results in a gain in constraining power of approximately 17% in the $\Omega_m - S_8$ parameter plane.

A different approach, the halo occupation distribution in the halo model, enables a connection between the masses of halos in which galaxies live and their large-scale bias. We use our constraints on linear bias parameters (along with the galaxy number density) and estimate the host halo masses of `redMaGiC` galaxies. We marginalize over the halo occupation distribution parameters and obtain 25% constraints on the mean mass of host halos. We show these constraints, including its evolution with redshift in Fig. 14, finding halo mass of approximately $1.5 \times 10^{13} M_\odot/h$ and its evolution with redshift consistent with the expected pseudo-evolution due to changing background density.

The 2 × 2pt combination of probes plays a crucial role in extracting the most cosmological information from LSS surveys, especially in constraining the matter content of universe (Ω_m) and the dark energy equation of state (w). In this analysis we measure the combination of galaxy clustering and galaxy-galaxy lensing at approximately 200σ; this significance is expected to dramatically increase with imminent large scale

surveys like the Euclid Space Telescope[5], the Dark Energy Spectroscopic Instrument[6], the Nancy G. Roman Space Telescope[7] and the Vera C. Rubin Observatory Legacy Survey of Space and Time.[8] In order to optimally analyze these high precision measurements, especially at non-linear small scales, we need better models and ensure their proper validation before applying them to measurements. We have shown that the hybrid perturbation theory galaxy bias model can be validated with simulations to sufficient accuracy for the present analysis. By relaxing the priors on all five parameters (per redshift bin), the model's accuracy can be improved though the increase in model complexity poses other challenges in parameter estimation. Finally, and perhaps most importantly, we have highlighted how understanding potential sources of systematic uncertainty is of paramount importance for extracting unbiased cosmological information in this era of precision cosmology.

---

[5] https://www.euclid-ec.org

[6] https://www.desi.lbl.gov

[7] https://roman.gsfc.nasa.gov

[8] https://www.lsst.org

[1] Abbott T., et al. 2018, Physical Review D, 98
[2] Abbott T., et al. 2020, Physical Review D, 102
[3] Aghanim N., et al. 2020, Astronomy & Astrophysics, 641, A6
[4] Amodeo S., et al. 2021, Physical Review D, 103
[5] Amon A., et al., 2021, To be submitted to PRD
[6] Baldauf T., et al. 2010, Physical Review D, 81
[7] Becker M. R., 2013, MNRAS, 435, 115
[8] Berlind A. A., Weinberg D. H., 2002, The Astrophysical Journal, 575, 587–616
[9] Bird S., Viel M., Haehnelt M. G., 2012, MNRAS, 420, 2551
[10] Blazek J., Vlah Z., Seljak U., 2015, Journal of Cosmology and Astroparticle Physics, 2015, 015–015
[11] Blazek J. A., et al. 2019, Physical Review D, 100
[12] Bridle S. L., et al. 2002, Monthly Notices of the Royal Astronomical Society, 335, 1193–1200
[13] Cacciato M., et al. 2009, Monthly Notices of the Royal Astronomical Society, 394, 929–946
[14] Cacciato M., et al. 2012, Monthly Notices of the Royal Astronomical Society, 426, 566–587
[15] Cacciato M., et al. 2013, Monthly Notices of the Royal Astronomical Society, 430, 767–786
[16] Cawthon R., et al., 2020, Submitted to MNRAS
[17] Clampitt J., et al. 2016, Monthly Notices of the Royal Astronomical Society, 465, 4204–4218
[18] Cooray A., Sheth R., 2002, Physics Reports, 372, 1–129
[19] Cordero J. P., Harrison I., et al., 2021, To be submitted to MNRAS
[20] Coupon J., et al. 2015, Monthly Notices of the Royal Astronomical Society, 449, 1352–1379
[21] Crocce M., Pueblas S., Scoccimarro R., 2012, 2LPTIC: 2nd-order Lagrangian Perturbation Theory Initial Conditions (ascl:1201.005)
[22] Crocce M., et al. 2015, Monthly Notices of the Royal Astronomical Society, 453, 1513–1530
[23] DES Collaboration 2021, To be submitted to PRD
[24] De Vicente J., Sánchez E., Sevilla-Noarbe I., 2016, MNRAS, 459, 3078
[25] DeRose J., et al. 2019, arXiv e-prints,
[26] DeRose J., et al., 2021a, To be submitted to MNRAS
[27] DeRose J., Becker M. R., Wechsler R. H., 2021b, arXiv e-prints, p. arXiv:2105.12104
[28] Desjacques V., Jeong D., Schmidt F., 2018, Physics Reports, 733, 1–193
[29] Diemer B., More S., Kravtsov A. V., 2013, The Astrophysical Journal, 766, 25
[30] Dvornik A., et al. 2018, Monthly Notices of the Royal Astronomical Society, 479, 1240–1259
[31] Elvin-Poole J., MacCrann N., et al., 2021, To be submitted to MNRAS
[32] Everett S., et al., 2020a, Submitted to ApJS
[33] Everett S., et al. 2020b, Dark Energy Survey Year 3 Results: Measuring the Survey Transfer Function with Balrog (arXiv:2012.12825)
[34] Fang X., Eifler T., Krause E., 2020a, arXiv e-prints, p. arXiv:2004.04833
[35] Fang X., et al. 2020b, JCAP, 2020, 010
[36] Feroz F., Hobson M. P., 2008, Monthly Notices of the Royal Astronomical Society, 384, 449–463
[37] Feroz F., Hobson M. P., Bridges M., 2009, Monthly Notices of the Royal Astronomical Society, 398, 1601–1614
[38] Feroz F., et al. 2019, The Open Journal of Astrophysics, 2
[39] Flaugher B., et al. 2015, The Astronomical Journal, 150, 150
[40] Fosalba P., et al. 2014, Monthly Notices of the Royal Astronomical Society, 447, 1319–1332
[41] Fosalba P., et al. 2015, Monthly Notices of the Royal Astronomical Society, 448, 2987–3000
[42] Friedrich O., et al., 2020, Submitted to MNRAS
[43] Fry J. N., Gaztanaga E., 1993, ApJ, 413, 447
[44] Gatti M., Giannini G., et al., 2020, Submitted to MNRAS
[45] Gatti M., Sheldon E., et al., 2021, Mon. Not. Roy. Astron. Soc.,

504, 4312

[46] Giannini G., et al., 2021, To be submitted to PRD

[47] Handley W. J., Hobson M. P., Lasenby A. N., 2015, Monthly Notices of the Royal Astronomical Society: Letters, 450, L61–L65

[48] Hang Q., et al. 2020, Monthly Notices of the Royal Astronomical Society, 501, 1481–1498

[49] Harris C. R., et al. 2020, Nature, 585, 357–362

[50] Hartley W. G., Choi A., et al., 2020, Submitted to MNRAS

[51] Heymans C., et al. 2021, Astronomy & Astrophysics, 646, A140

[52] Hikage C., et al. 2019, Publications of the Astronomical Society of Japan, 71

[53] Howlett C., et al. 2012, JCAP, 1204, 027

[54] Huff E., Mandelbaum R., 2017, Metacalibration: Direct Self-Calibration of Biases in Shear Measurement (arXiv:1702.02600)

[55] Hunter J. D., 2007, Computing in Science Engineering, 9, 90

[56] Huterer D., Turner M. S., 2001, Physical Review D, 64

[57] Jarvis M., Bernstein G., Jain B., 2004, Monthly Notices of the Royal Astronomical Society, 352, 338–352

[58] Jarvis M., et al., 2021, Mon. Not. Roy. Astron. Soc., 501, 1282

[59] Joachimi B., et al. 2021, Astronomy & Astrophysics, 646, A129

[60] Kitanidis E., White M., 2020, Monthly Notices of the Royal Astronomical Society, 501, 6181–6198

[61] Krause E., Eifler T., 2017a, Mon. Not. Roy. Astron. Soc., 470, 2100

[62] Krause E., Eifler T., 2017b, Monthly Notices of the Royal Astronomical Society, 470, 2100–2112

[63] Krause E., et al. 2017, preprint, (arXiv:1706.09359)

[64] Krause E., et al., 2021, To be submitted to PRD

[65] Krolewski A., Ferraro S., White M., 2021, Cosmological constraints from unWISE and Planck CMB lensing tomography (arXiv:2105.03421)

[66] Kwan J., et al. 2016, Monthly Notices of the Royal Astronomical Society, 464, 4045–4062

[67] Landy S. D., Szalay A. S., 1993, ApJ, 412, 64

[68] Lange J. U., et al. 2021, Monthly Notices of the Royal Astronomical Society, 502, 2074–2086

[69] Le Brun A. M. C., et al. 2014, Monthly Notices of the Royal Astronomical Society, 441, 1270–1290

[70] Leauthaud A., et al. 2017, Monthly Notices of the Royal Astronomical Society, 467, 3024–3047

[71] Lemos P. Raveri M., et al., 2020, Submitted to MNRAS

[72] Lemos P., et al., 2021, To be submitted to MNRAS

[73] Lewis A., 2019

[74] Lewis A., Bridle S., 2002, Phys. Rev. D, 66, 103511

[75] Lewis A., Challinor A., Lasenby A., 2000, ApJ, 538, 473

[76] Limber D. N., 1953, ApJ, 117, 134

[77] LoVerde M., Afshordi N., 2008, Phys. Rev. D, 78, 123506

[78] MacCrann N., et al., 2020a, Submitted to MNRAS

[79] MacCrann N., et al. 2020b, Mon. Not. Roy. Astron. Soc., 491, 5498

[80] Mandelbaum R., et al. 2013, Monthly Notices of the Royal Astronomical Society, 432, 1544–1575

[81] McDonald P., Roy A., 2009, Journal of Cosmology and Astroparticle Physics, 2009, 020

[82] More S., et al. 2015, The Astrophysical Journal, 806, 2

[83] Morganson E., et al. 2018a, Publications of the Astronomical Society of the Pacific, 130, 074501

[84] Morganson E., et al. 2018b, PASP, 130, 074501

[85] Myles J., Alarcon A., et al., 2020, Submitted to MNRAS

[86] Navarro J. F., Frenk C. S., White S. D. M., 1996, The Astrophysical Journal, 462, 563

[87] Pandey S., et al. 2020, Perturbation theory for modeling galaxy bias: validation with simulations of the Dark Energy Survey (arXiv:2008.05991)

[88] Philcox O. H., et al. 2020, Journal of Cosmology and Astroparticle Physics, 2020, 032–032

[89] Porredon A., et al., 2021a, To be submitted to PRD

[90] Porredon A., et al., 2021b, Phys. Rev. D, 103, 043503

[91] Prat J., et al. 2018, Physical Review D, 98

[92] Prat J., et al., 2021, To be submitted to PRD

[93] Rodríguez-Monroy M., et al., 2021, To be submitted to MNRAS

[94] Rozo E., et al. 2016, Monthly Notices of the Royal Astronomical Society, 461, 1431–1450

[95] Saito S., et al. 2014, Physical Review D - Particles, Fields, Gravitation and Cosmology, 90, 1

[96] Samuroff S., et al. 2019, Monthly Notices of the Royal Astronomical Society, 489, 5453–5482

[97] Sánchez C., Prat J., et al., 2021, To be submitted to PRD

[98] Scherrer R. J., Weinberg D. H., 1998, ApJ, 504, 607

[99] Secco L. F., Samuroff S., et al., 2021, To be submitted to PRD

[100] Sevilla-Noarbe I., et al., 2020, Submitted to ApJS

[101] Sevilla I., et al. 2011, arXiv e-prints, p. arXiv:1109.6741

[102] Sheldon E. S., Huff E. M., 2017, The Astrophysical Journal, 841, 24

[103] Singh S., et al. 2017, Monthly Notices of the Royal Astronomical Society, 471, 3827–3844

[104] Singh S., et al. 2019, Monthly Notices of the Royal Astronomical Society, 491, 51–68

[105] Springel V., et al. 2005, Nature, 435, 629–636

[106] Suchyta E., et al. 2016, Monthly Notices of the Royal Astronomical Society, 457, 786–808

[107] Takahashi R., et al. 2012, Astrophys. J., 761, 152

[108] Tinker J., et al. 2008, The Astrophysical Journal, 688, 709–728

[109] Tinker J. L., et al. 2010, The Astrophysical Journal, 724, 878–886

[110] To C., et al. 2021, Physical Review Letters, 126

[111] Troxel M., et al. 2018, Physical Review D, 98

[112] Virtanen P., et al. 2020, Nature Methods, 17, 261

[113] Wang Y., 2008, Physical Review D, 77

[114] Wechsler R. H., et al. 2021, arXiv e-prints, p. arXiv:2105.12105

[115] Wibking B. D., et al. 2018, Monthly Notices of the Royal Astronomical Society, 484, 989–1006

[116] Wibking B. D., et al. 2019, Monthly Notices of the Royal Astronomical Society, 492, 2872–2896

[117] Yuan S., Eisenstein D. J., Leauthaud A., 2020, Monthly Notices of the Royal Astronomical Society, 493, 5551–5564

[118] Zacharegkas, G. et al. prep.

[119] Zehavi I., et al. 2011, The Astrophysical Journal, 736, 59

[120] Zheng Z., et al. 2005, The Astrophysical Journal, 633, 791–809

[121] Zu Y., 2020, On the "Lensing is Low" of BOSS Galaxies (arXiv:2010.01143)

[122] Zuntz J., et al. 2015, Astronomy and Computing, 12, 45–59

[123] van den Bosch F. C., et al. 2013, Monthly Notices of the Royal Astronomical Society, 430, 725–746

Appendix A: Point mass marginalization

The point mass parameter (B) can also be expressed as residual mass bias, $B = \delta M / \pi$ where δM is approximately related to the difference between the model and true estimate

of halo mass below the scales of our model validity (r_{min}). More accurately, δM_{halo} can be expressed in terms of galaxy-matter correlation as:

$$\delta M = \int_0^{r_{min}} dr_p (2\pi r_p) \int_{-\infty}^{\infty} d\Pi \, \Delta\xi_{gm}\left(\sqrt{r_p^2 + \Pi^2}, z\right), \quad (A1)$$

where $\Delta\xi_{gm} = \xi_{gm}^{true} - \xi_{gm}^{model}$.

In Fig. 15 we compare the constraining power of 2×2pt and 3×2pt *simulated* analysis at our *fiducial* scale cuts for different point mass parameter settings. We generate a noiseless theory baseline datavector using the linear bias model and the *fiducial* parameter values given in Table I. In the blue and red filled contours, instead of analytically marginalizing over the point mass parameters, we explicitly sample them when analyzing 2×2pt and 3×2pt datavectors respectively. To test the impact of point mass marginalization on the constraining power, we also show the constraints obtained after fixing the PM parameters to their fiducial value of zero using unfilled contours. The black and green unfilled contours show the constraints using 2×2pt and 3×2pt datavectors respectively. We see that although point mass marginalization has a significant impact on the constraining power of the 2×2pt analysis, it has a small impact on the 3×2pt analysis. The main reason is that, due to extra constraints from cosmic shear, we break the degeneracy between PM parameters and cosmological parameters, and hence uncertainty in PM parameters do not dilute our cosmology constraints.

As PM marginalization degrades the constraining power of 2×2pt significantly, it might be desirable to implement an informative prior on the PM parameters. However, motivating an astrophysical prior on the PM parameters is not possible for our scale cuts as the majority of residual mass constraints are contributed from the 2-halo regime, as shown in Fig. 16. For simplicity, we assume all our galaxies occupy the center of $2.5 \times 10^{13} M_{\odot}/h$ mass halos. The input "truth" curve in black solid line uses ξ_{gm} that is generated using the Navarro-Frenk-White profile [86] in the 1-halo regime ($r < 0.5$ Mpc/h) and one–loop PT in the 2-halo regime ($r > 0.5$ Mpc/h). Given this input halo mass, the halo model framework predicts the effective large scale linear bias value [18]. The dashed blue curve is generated using a linear bias model, using a linear bias value that is 1σ lower from this predicted value. Here σ is the uncertainty obtained from 2×2pt marginalized constraints on the galaxy bias for first tomographic bin. The area between the two curves below some scale is equal to total δM as calculated using Eq. A1.

We show the contribution to δM separately for the 1-halo region (below the red dashed line) and 2-halo regimes (up to the scales of 6Mpc/h, which are our scale cuts for $\gamma_t(\theta)$). We find that the 2-halo regime contributes significantly more than the 1-halo region and the resulting δM value is significantly more than the input halo mass of $2.5 \times 10^{13} M_{\odot}/h$. An informative prior would amount to understanding the galaxy-matter correlation and its dependence on cosmology and galaxy bias model from all scales below our scale cuts. Therefore we choose an uninformative wide prior on the point mass parameters.

The baseline model parameterization assumes the point mass parameter to be constant within each tomographic bin.
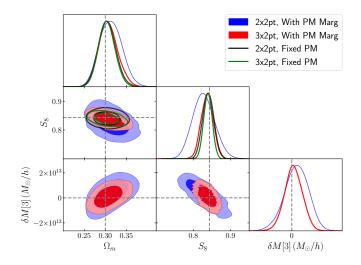

Figure 15. Effect of point mass marginalization on the constraining power of 2×2pt and 3×2pt. We see that the constraining power of 2×2pt degrades significantly with point mass marginalization, while for 3×2pt the change is minimal. Including the shear-shear correlation breaks the degeneracy between point-mass (we show PM for third bin, $M_{halo}[3]$) and S_8, leading to smaller sensitivity of cosmology constraints on point mass constraints.
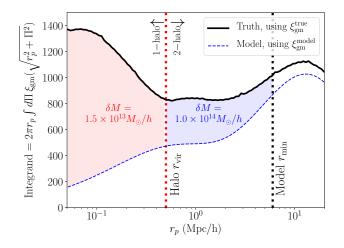

Figure 16. We show the contribution to the residual mass shown in Eq. A1 from different radial regimes. We find a significant contribution from 2-halo regime and therefore we cannot motivate an astrophysical informative prior on the PM parameters, without putting an informative prior on cosmology as well.

We test this assumption implicitly in the suite of Buzzard simulations. The datavector measured in N-body Buzzard simulation will capture the effects of evolving point-mass parameters due to the evolution of the galaxy-matter correlation within a lens tomographic bin. As we have validated that our scale cuts pass our threshold criteria of bias in cosmological parameters being less than 0.3σ, we can conclude that the effect of point mass parameter evolution is small. Here we also test this effect explicitly by generating a simulated galaxy matter correlation function using the halo model. We assume a
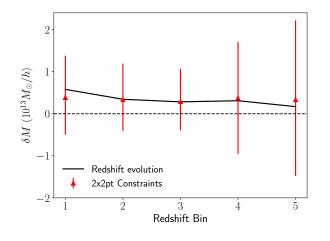
Figure 17. We show the effect of the evolution of galaxy matter correlation functions on the PM parameters for each tomographic bin in the black line. The red errorbars show the expected errorbars on PM parameters for 2×2pt as shown in Fig. 15. The blue errorbars are the constraints from 3×2pt.

constant HOD of the `redMaGiC` galaxies but include the evolution of halo mass function and halo bias to predict the evolution of the galaxy-matter correlation function. The contribution to the PM parameter due to this evolution in each tomographic bin is given by Eq. A1. In Fig. 17, we show this contribution to each redshift bin by the black solid line. We compare this bias with the expected level of uncertainty in the PM parameters by plotting the marginalized constraints on these parameters as shown in Fig. 15 for both 2×2pt and 3×2pt analyses. We see that the uncertainty in PM parameters is significantly greater than the expected bias.

Appendix B: Datavector residuals

We show the comparison between our measurements and best-fit theory datavector in Fig. 18. We show the residuals between data and best-fit theory model from both the *fiducial* model as well as with $X_{\text{lens}} = 0.87$ model . Using the *fiducial* linear bias model scale cuts of $(8,6)$ Mpc/h (that leaves 302 datapoints in total), we find a minimum χ^2 of 347.2 and 351.1 for the *fiducial* model and $X_{\text{lens}} = 0.87$ model respectively.

Appendix C: Halo mass inference

In this section we detail the methodology to infer the host halo mass of our `redMaGiC` lens galaxy sample from the constraints on galaxy bias parameters and number density. We use the halo model framework to make this prediction and parameterize the number of galaxies in a halo of mass M in

tomographic bin j as $N_g^j(M) = N_{\text{cen}}^j(M) + N_{\text{sat}}^j(M)$ where N_{cen}^j is the number of central galaxies and N_{sat}^j is the number of satellite galaxies. We parameterize these two components as:

$$N_{\text{cen}}^j = \frac{f_{\text{cen}}^j}{2}\left[1 + \text{erf}\left(\frac{\log M - (\log M_{\min})^j}{(\sigma_{\log M})^j}\right)\right] \quad (C1)$$

$$N_{\text{sat}}^j = \frac{1}{2}\left[1 + \text{erf}\left(\frac{\log M - (\log M_{\min})^j}{(\sigma_{\log M})^j}\right)\right] \times \left(\frac{M_{\text{h}}}{M_1^j}\right)^{\alpha^j}. \quad (C2)$$

Here we have five free parameters, f_{cen}^j, $(\log M_{\min})^j$, $(\sigma_{\log M})^j$, M_1^j and α^j, that we marginalize over. We can predict the comoving number density $(\overline{n}(z)^j)$ and galaxy bias for a given tomographic bin j, b_1^j, from galaxy HOD as follows:

$$\overline{n}^j(z) = \int_0^\infty dM \frac{dn}{dM} N_g^j(M)$$

$$b_1^j = \int dz \frac{n_g^j(z)}{\overline{n}^j(z)} \int_0^\infty dM \frac{dn}{dM} N_g^j(M) b_1^{\text{halo}}(M, z)$$

$$(C3)$$

We use the [108] halo mass function (dn/dM) and the [109] relation for linear halo bias ($b_1^{\text{halo}}(M, z)$).

Therefore, Eqs. C3 allow us to predict the number density and galaxy bias values. We then sample these HOD parameters to fit the datavector $\vec{\mathcal{D}}_H = \overline{n}^j(z_1)...\overline{n}^j(z_n), b_1^j, b_2^j]$ of length d where $\overline{n}^j(z_1)...\overline{n}^j(z_n)$ are the $n = d - 2$ observed comoving number density of `redMaGiC` galaxies as shown in middle panel of Fig.19 and b_1^j and b_2^j are the marginalized mean bias values obtained at our *fiducial* scale cut. For a given set of HOD parameters (Θ_H), the theoretical prediction is given by $\mathcal{T}_H$ and we write our log-likelihood as:

$$\ln \mathcal{L}(\vec{\mathcal{D}}_H | \Theta) = -\frac{1}{2}\left[(\vec{\mathcal{D}}_H - \vec{\mathcal{T}}_H(\Theta_H)) \, \mathcal{C}_H^{-1} \, (\vec{\mathcal{D}}_H - \vec{\mathcal{T}}_H(\Theta_H))^{\text{T}}\right.$$

$$\left. - \ln(|\mathcal{C}_H|)\right] \quad (C4)$$

In order to account for variation of HOD within a tomographic bin that contributes to the variation on $\overline{n}^j(z)$ within each tomographic bin as seen in Fig.19, we implement an analytical marginalization scheme. We change the covariance of our datavector $\mathcal{C}_H$ as :

$$\mathcal{C}_H \rightarrow \mathcal{C}_H + \alpha_c \mathcal{I}_D \quad (C5)$$

where $\mathcal{I}_D$ is a diagonal matrix of dimension $d \times d$ whose diagonal elements equal to 1 from index 1 to d-1, and equal to 0 otherwise. We sample over the parameter α_c, treating it as a free parameter.
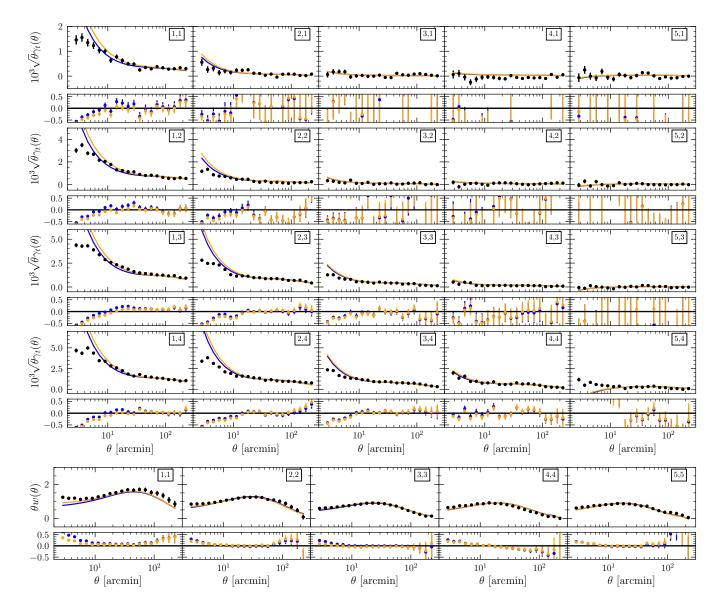
Figure 18. The measurements of $w(\theta)$ and $\gamma_t(\theta)$ with `redMaGiC` sample are shown with black dots. We show the best fit using the *fiducial Linear bias* model in blue and model with $X_{\text{lens}} = 0.87$ in orange.
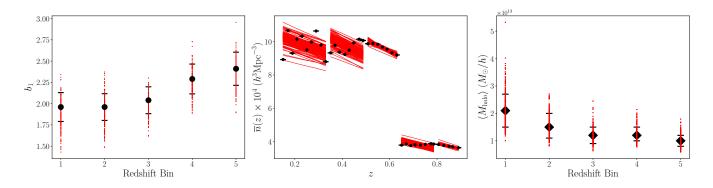

Figure 19. This figure shows the marginalized constraints on the large-scale bias of `redMaGiC` sample for the five tomographic bins on the left panel. The black dots denote the mean, and the error bars correspond to 68% credible interval. Using these constraints and co-moving number density (middle panel), we infer the constraints on mean halo mass, as shown in the right panel for five tomographic bins. The red line and dots correspond to MCMC samples. We use the *Linear bias* model with $X_{\text{lens}} = 0.87$.